



Supplementary Materials for

Global glacier change in the 21st century: Every increase in temperature matters

David R. Rounce *et al.*

Corresponding author: David R. Rounce, drounce@cmu.edu

Science **379**, 78 (2023)
DOI: 10.1126/science.abo1324

The PDF file includes:

Methods
Figs. S1 to S28
Tables S1 to S5
References

Methods

Glacier data

Glacier outlines of all ~215,000 glaciers covering an area of 705,739 km² are provided by the Randolph Glacier Inventory (RGI, version 6) (23). Glacier-wide geodetic mass change rates for each glacier from 2000 to 2019 (1) are used for model calibration. Frontal ablation data from 2000 to 2020 in the Northern Hemisphere (13), South America (12), and Antarctica (10, 11) are used to calibrate marine-terminating glaciers. Annual and seasonal glaciological glacier-wide mass balance data from 1979 to 2019 (32) are used for model validation (Figs. S23-26). Spatially distributed sub-debris melt enhancement factors for all debris-covered glaciers (17) are used to account for the enhanced or suppressed melting due to debris thickness. The Open Global Glacier Model (OGGM) (7) was used to compile these data sets with a digital elevation model for each glacier to bin the data according to the glacier central flowlines. OGGM is also used to estimate each glacier's initial ice thickness, while ensuring that each region's total glacier volume matches the regional multi-model ice thickness estimates (18) (see Model calibration).

Climate data

Monthly near-surface air temperature and precipitation data from ERA5 (33) are used for historical (1980-2019) simulations. Air temperature lapse rates are estimated using monthly air temperature data from various pressure levels.

An ensemble of ten GCMs and three RCPs (RCP2.6, RCP4.5, and RCP8.5), i.e., the same as those used by GlacierMIP (2), and an ensemble of 12 GCMs forced by four SSPs (SSP1-2.6, SSP2-4.5, SSP3-7.0, and SSP5-8.5) are used for the projections (Table S3). Future simulations are adjusted using additive factors for air temperature and multiplicative factors for precipitation to remove any bias between the GCMs and ERA5 data over the calibration period (2000-2019) (14, 15).

Following the Intergovernmental Panel on Climate Change (34), mean global temperature change from 2081-2100 compared to pre-industrial levels is computed by adding the observed increase of +0.63°C from 1850-1900 until 1986-2005 to each GCM's projected temperature increase between 1986-2005 and 2081-2100. Four GCMs also provided data for SSP1-1.9, which are used to provide additional forcing for low mean global temperature change scenarios. Projections are aggregated into +1.5°C, +2°C, +3°C, and +4°C temperature change scenarios based on the global mean temperature change for each combination of GCM and emission scenario with a tolerance of ±0.25 for the 1.5°C scenario and ±0.5 for all others.

Glacier modeling

The glacier evolution model is a hybrid model that uses the mass balance module of the Python Glacier Evolution Model (PyGEM) (14, 15) and the glacier dynamics module from OGGM (7) to model every glacier independently from 2000-2100 for various ensembles of GCMs, SSPs, and RCPs. The model computes the climatic mass balance (i.e., snow accumulation minus melt plus refreezing) for each surface elevation bin using a monthly time step. The model computes glacier melt using a degree-day model, accumulation using a temperature threshold, and refreezing based on the annual air temperature (14, 15). Glacier geometry is updated annually using a flowline model based on the Shallow-Ice Approximation to explicitly account for glacier dynamics (7) using a density of 900 kg m⁻³ for converting mass to volume. For marine-terminating glaciers, frontal ablation is modeled using a frontal ablation parameterization coupled to the ice dynamical model. Mass is removed at the glacier front when the bedrock is below sea level using an empirical formula (35). Mass changes are converted to

sea-level change using an ocean area of $3.625 \times 10^8 \text{ km}^2$ (36). The glacier contribution to sea-level rise is corrected to account for the effect of grounded ice below sea level displacing ocean water for marine-terminating glaciers (8).

Model calibration

The mass balance model uses three parameters, i.e., temperature bias, precipitation factor, and degree-day factor of snow (a ratio of 0.7 between the degree-day factor of snow and ice is used to estimate the factor for ice), that are assumed constant in time. The temperature bias and precipitation factor downscale the GCM data to the glacier-scale, and the degree-day factors control melt rates. Bayesian inference is used to calibrate the three parameters for each glacier based on Markov Chain Monte Carlo (MCMC) methods (14, 15) with geodetic mass balance data from 2000-2019 (1) and a mass balance emulator for each glacier. An independent emulator for each glacier was derived by performing 100 present-day simulations based on randomly sampled model parameter sets and then fitting a Gaussian Process to these parameter-response pairs. This model was then substituted for PyGEM within the MCMC sampler, which reduced the computational expense by two orders of magnitude. For all Gaussian process emulators, we use the squared-exponential covariance function, which has hyperparameters controlling the characteristic amplitude and correlation length scale, along with a Gaussian likelihood model (with observation noise hyperparameter) and a constant mean. We optimize hyperparameters by maximizing the marginal log-likelihood (37) using the Adam optimizer (38).

A comparison of the MCMC methods using the emulator versus full model simulations for a subset of 2500 randomly selected glaciers was performed. The posterior predictive distribution of the mass balance and marginal posterior distributions of the temperature bias, precipitation factor, and degree-day factor of snow agree well, especially for glaciers with an initial area greater than 1 km^2 (Fig. S27). Specifically, 95% of the differences in the median of the posterior predictive distribution for the mass balance are between -0.06 to $0.04 \text{ m w.e. yr}^{-1}$, which is well below the mean uncertainty associated with the geodetic mass balance data ($0.27 \text{ m w.e. yr}^{-1}$) (Hugonet et al. 2021). The differences for the marginal posterior distributions of the temperature bias are -0.45 to 0.64°C , precipitation factor are -0.32 to 0.35, and the degree-day factor of snow are -0.57 to $0.70 \text{ mm w.e. d}^{-1} \text{ }^\circ\text{C}^{-1}$. These differences in the marginal distribution are less than the normalized median absolute deviation associated with the full simulation for each parameter (0.86°C for the temperature bias; 0.55 for the precipitation factor; and $1.29 \text{ mm w.e. d}^{-1} \text{ }^\circ\text{C}^{-1}$ for the degree-day factor of snow). Given that most glaciers smaller than 1 km^2 are projected to completely disappear regardless of the future climatic forcing, the use of emulators should have minimal impact on the projections.

The prior distributions for the degree-day factor were based on previous data (39), while the temperature bias and precipitation factor were derived using a simple optimization scheme (14), which provides an approximation of the regional joint prior distribution for each RGI Order 2 subregion. The temperature bias assumes a normal distribution and the precipitation factor assumes a gamma distribution to ensure positivity. Glacier-wide winter mass balance data (32) were used to determine a reasonable upper-level constraint for the precipitation factor for the simple optimization scheme.

The glacier dynamics model relies on a single parameter (ice viscosity) that is calibrated at the regional level to match the multi-model ice volume estimates (18). The same value is then used for the projections. In future simulations, the initial ice thickness is estimated for each glacier, GCM, scenario, and set of model parameters using a mass-conservation inversion approach (7), which enables the simulations to account for uncertainty associated with the initial

ice thickness (Table S4). The uncertainty associated with the initial ice thickness varies regionally ranging from ± 2 to $\pm 9\%$. This range of uncertainty captures most of the regional differences between a recent estimate of ice thickness (40) compared to the multi-model “consensus” estimate (18) used in our study. In regions where differences are larger (e.g., High Mountain Asia, Greenland Periphery), one can expect the glacier contribution to sea-level to vary by roughly the same percentage as the differences in initial volume (8).

Marine-terminating glaciers

Marine-terminating glaciers have an additional frontal ablation parameter that is assumed constant in time and calibrated for each individual glacier to match frontal ablation data (10–13) (Fig. S28). The frontal ablation calibration is performed independently of the Bayesian calibration scheme to avoid circularity issues associated with the frontal ablation, climatic mass balance, and ice thickness inversion. The optimization is performed using a bisection method. The initial ice thickness is estimated using the mass balance parameters assuming the glacier is land-terminating. Then a forward simulation from 2000–2019 is run to estimate the frontal ablation. If a dynamic instability error occurs during the forward simulation (8% of glaciers), the glacier dynamics model uses mass redistribution curves instead (8, 15). Uncertainty associated with the frontal ablation parameter is estimated by performing the optimization to match ± 1 standard deviation of the frontal ablation data (10–13). The frontal ablation parameter is assumed to have a truncated normal distribution based on the mean, standard deviation, and lower and upper bounds of 0.001 and 5 (8). For quality control, we combined the frontal ablation and geodetic mass balance observations to estimate climatic mass balances (36). For some glaciers, the resulting climatic mass balances are unrealistic due to errors in the RGI outlines and/or poor glacier thickness and velocity data used in frontal ablation calculations. For these glaciers, we assume frontal ablation is overestimated and reduce the frontal ablation to ensure the climatic mass balance is within three standard deviations of the regional mean from the geodetic mass balance data. The Antarctic and Subantarctic region has the sparsest frontal ablation data, so the region’s median frontal ablation parameter and corresponding standard deviation is used for glaciers that lack frontal ablation data.

Inclusion of frontal ablation when estimating initial ice thickness increases the mass of ice (41), globally by 16% and regionally from less than 1% (Arctic Canada North) to 48% (Antarctic and Subantarctic), compared to excluding frontal ablation. The increase in initial ice thickness primarily occurs at the glacier terminus such that 57% of the additional mass is below sea level. Globally, the percentage of mass below sea level increases from 10% (excluding frontal ablation) to 17% (including frontal ablation) and the initial mass in units of potential sea-level equivalent increases by 23 mm SLE when including frontal ablation.

Model uncertainty

For each GCM and future climate scenario (RCP or SSP), 50 simulations are run based on the posterior distributions from the Bayesian inference to account for model parameter uncertainty. Regional results are derived by aggregating the median of these individual glacier runs and uncertainty is shown as the ensemble median and 95% confidence interval for each scenario. The only exception is the uncertainty associated with the annual frontal ablation rates. Since the frontal ablation parameterization is insensitive to temperature and precipitation forcing and not coupled to an ocean model, the multi-GCM uncertainty underestimates the actual uncertainty. Instead, the 95% confidence interval accompanying the mean annual frontal ablation rate is based on the model parameter uncertainty assuming glacier frontal ablation rates are perfectly correlated within the same region and individual regions are independent.

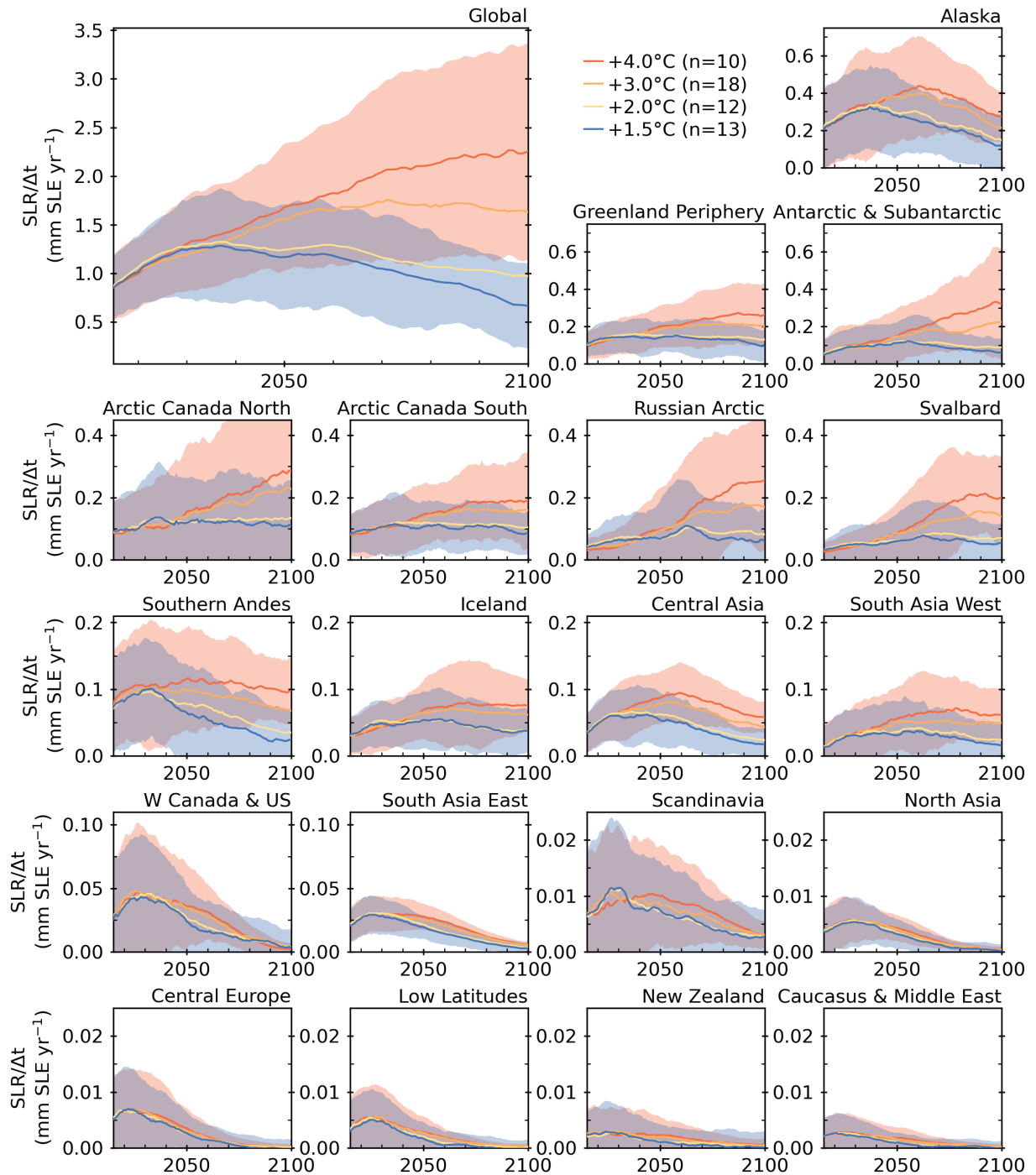


Fig. S1.

Global and regional rates of glacier contribution to sea-level change from 2015 to 2100 for global temperature change scenarios in 2100 relative to pre-industrial levels. Colors depict the ensemble median and shading indicates the 95% confidence interval (shown only for the +1.5°C and +4°C scenarios). The number of glacier projections with different GCMs and SSP scenarios that fall into each temperature change scenario is shown in the legend. Regions are ordered by their total mass loss. Note the scale varies among panels.

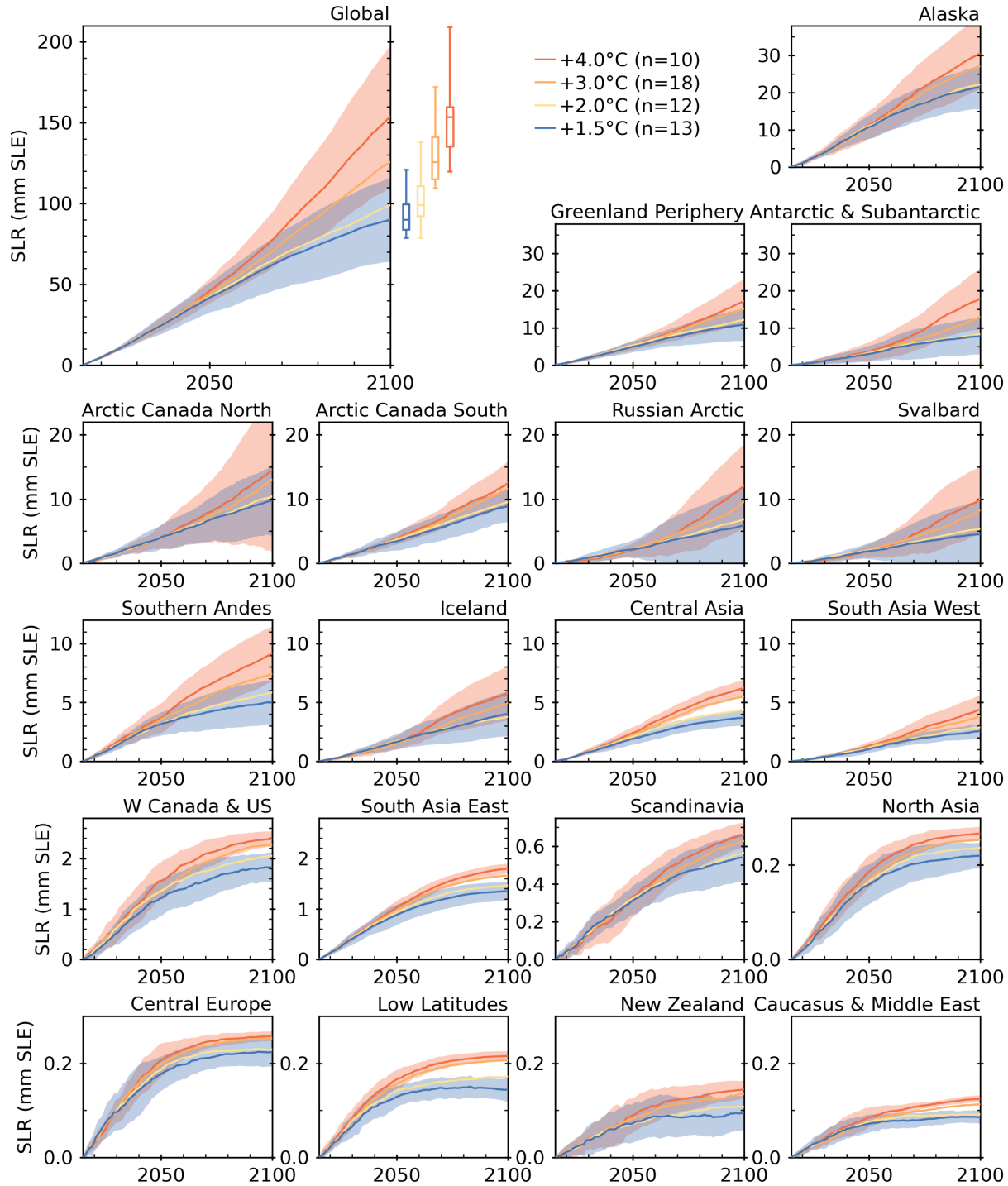


Fig. S2.

Global and regional projections of the cumulative contribution from annual glacier mass change to sea level rise (SLR) from 2015 to 2100 for global temperature change scenarios. Colors depict the ensemble median and shading indicates the 95% confidence interval (shown only for the +1.5°C and +4°C scenarios). The number of glacier projections with different GCMs and SSP scenarios that fall into each temperature change scenario is shown in the legend. Regions are ordered by their total mass loss. Note the scale varies among panels.

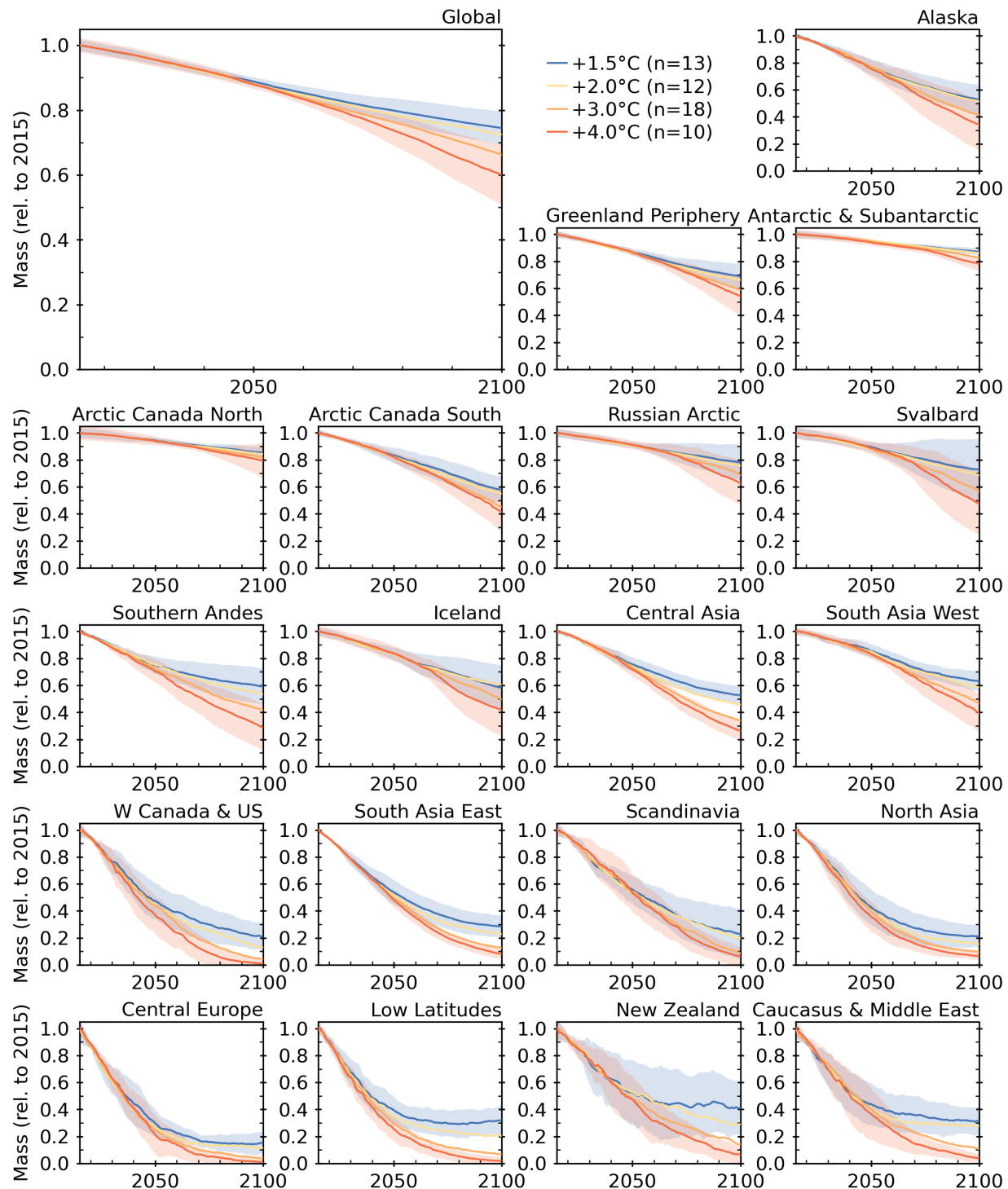


Fig. S3.

Global and regional mass from 2015 to 2100, relative to 2015, for global temperature change scenarios. Colors depict the ensemble median and shading indicates the 95% confidence interval (shown only for the +1.5°C and +4°C scenarios). The number of glacier projections with different GCMs and SSP scenarios that fall into each temperature change scenario is shown in the legend. Regions are ordered by their total mass loss.

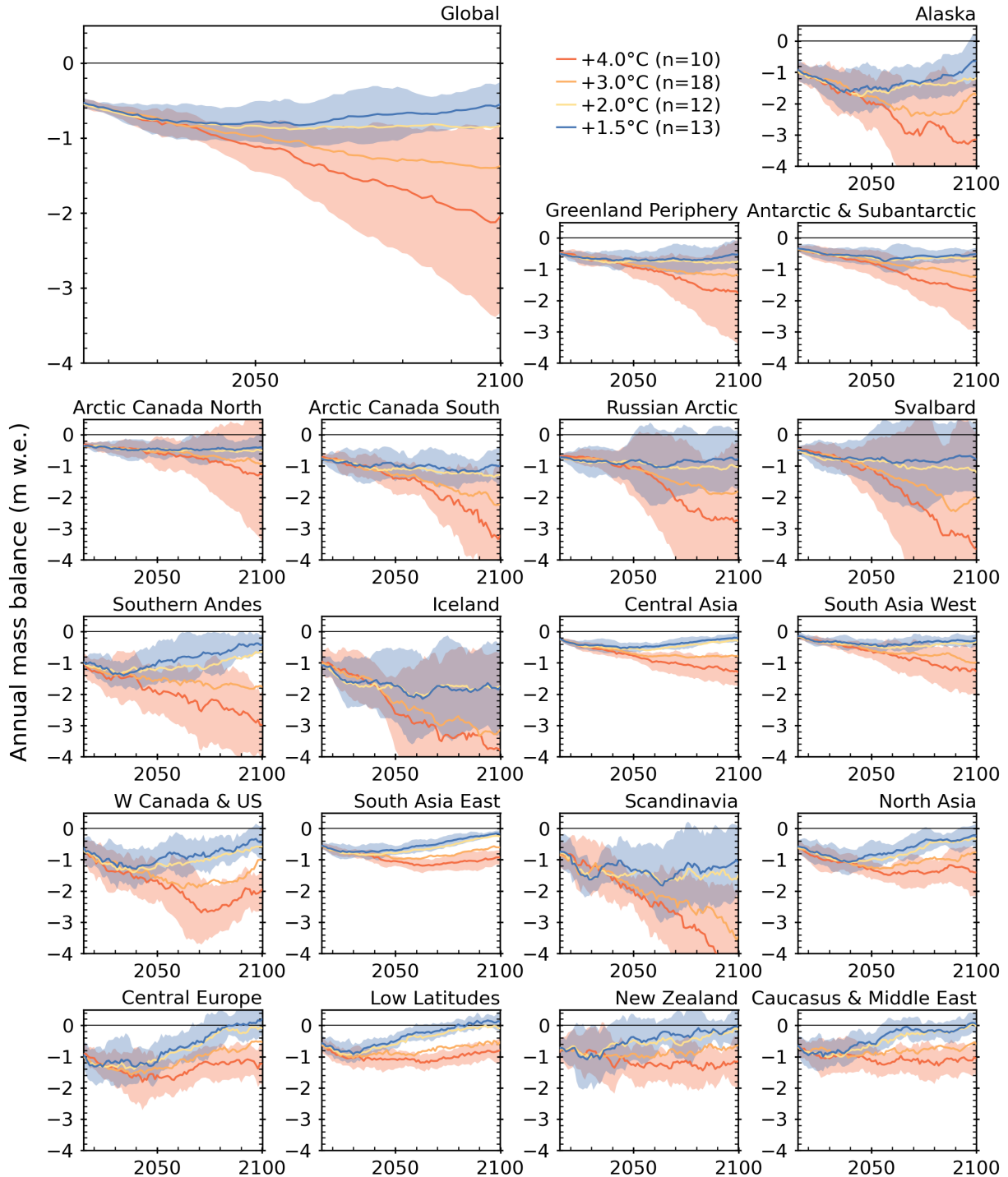


Fig. S4.

Global and regional area-averaged annual glacier mass balance from 2015 to 2100 for global temperature change scenarios in 2100 relative to pre-industrial levels. Colors depict the ensemble median and shading indicates the 95% confidence interval (shown only for the +1.5°C and +4°C scenarios). An 11-year running mean is used to reduce variability in individual years. The number of glacier projections with different GCMs and SSP scenarios that fall into each temperature change scenario is shown in the legend. Regions are ordered by their total mass loss.

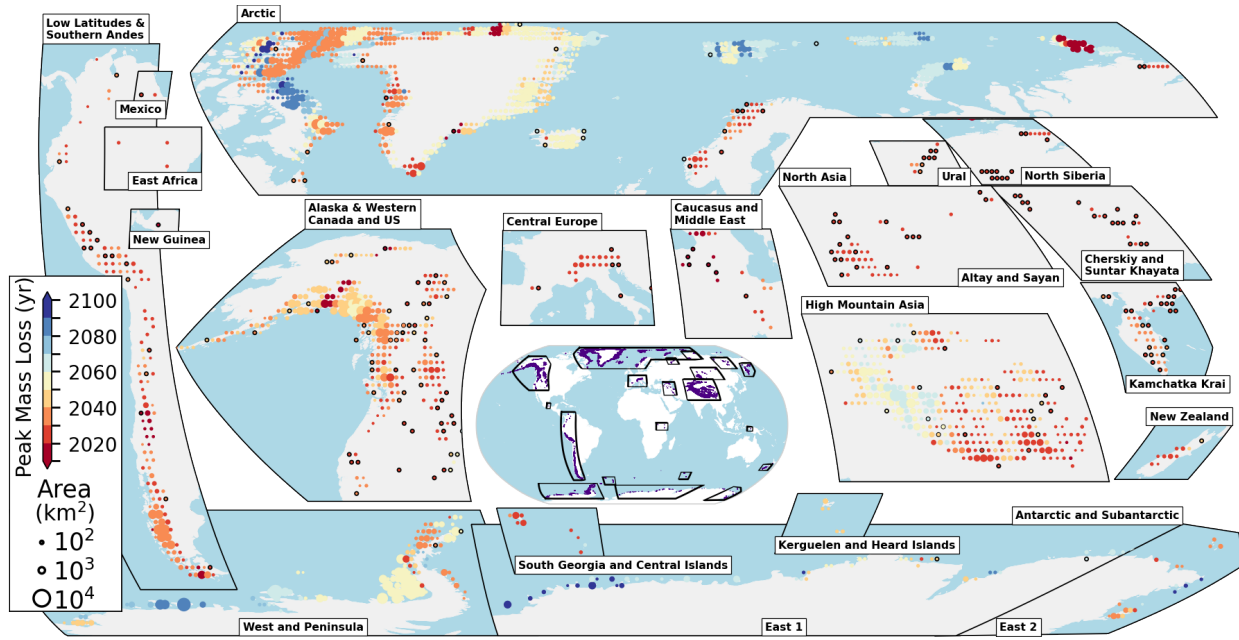


Fig. S5.

Spatial distribution of the year of maximum annual glacier mass loss (Gt) for +1.5°C. Tiles are aggregated by $1^\circ \times 1^\circ$ below 60° latitude, $2^\circ \times 1^\circ$ between 60° and 74° latitude and $2^\circ \times 2^\circ$ above 74° latitude to represent approximately 10,000 km 2 each. Circles are scaled based on glacierized area in 2015 and are colored by the year of maximum mass loss. Tiles that have experienced complete deglaciation by 2100 are marked by black circles. An 11-year running mean is used to reduce variability in individual years.

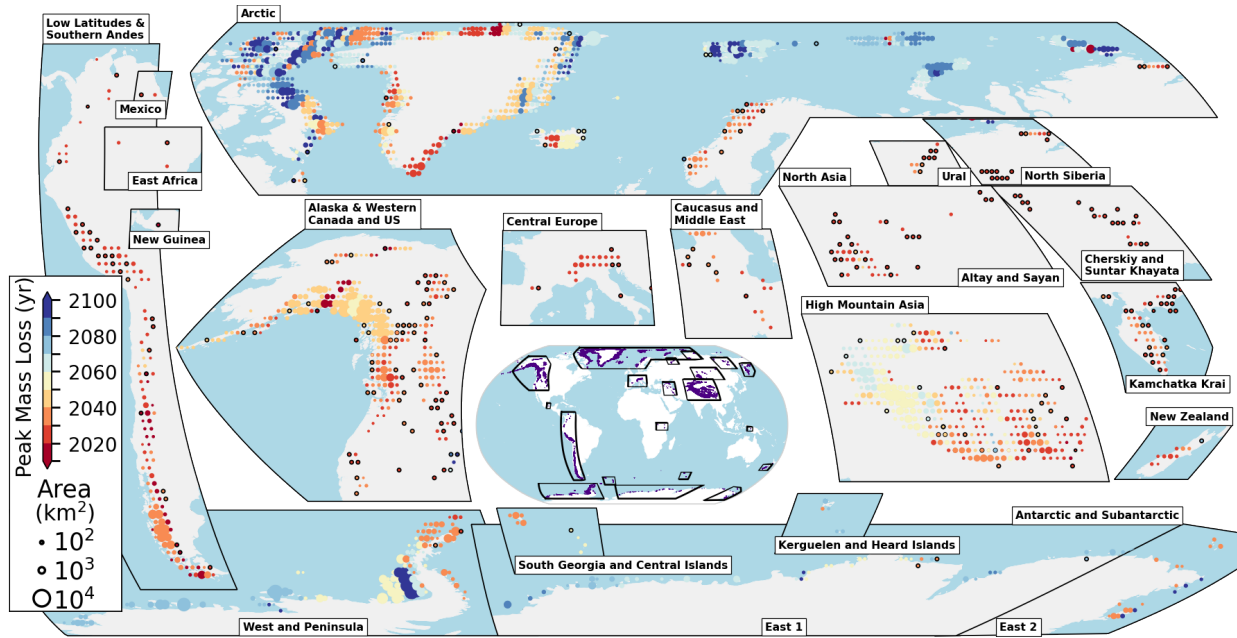


Fig. S6.

Spatial distribution of the year of maximum annual glacier mass loss (Gt) for +2°C. Tiles are aggregated by $1^\circ \times 1^\circ$ below 60° latitude, $2^\circ \times 1^\circ$ between 60° and 74° latitude and $2^\circ \times 2^\circ$ above 74° latitude to represent approximately 10,000 km 2 each. Circles are scaled based on glacierized area in 2015 and are colored by the year of maximum mass loss. Tiles that have experienced complete deglaciation by 2100 are marked by black circles. An 11-year running mean is used to reduce variability in individual years.

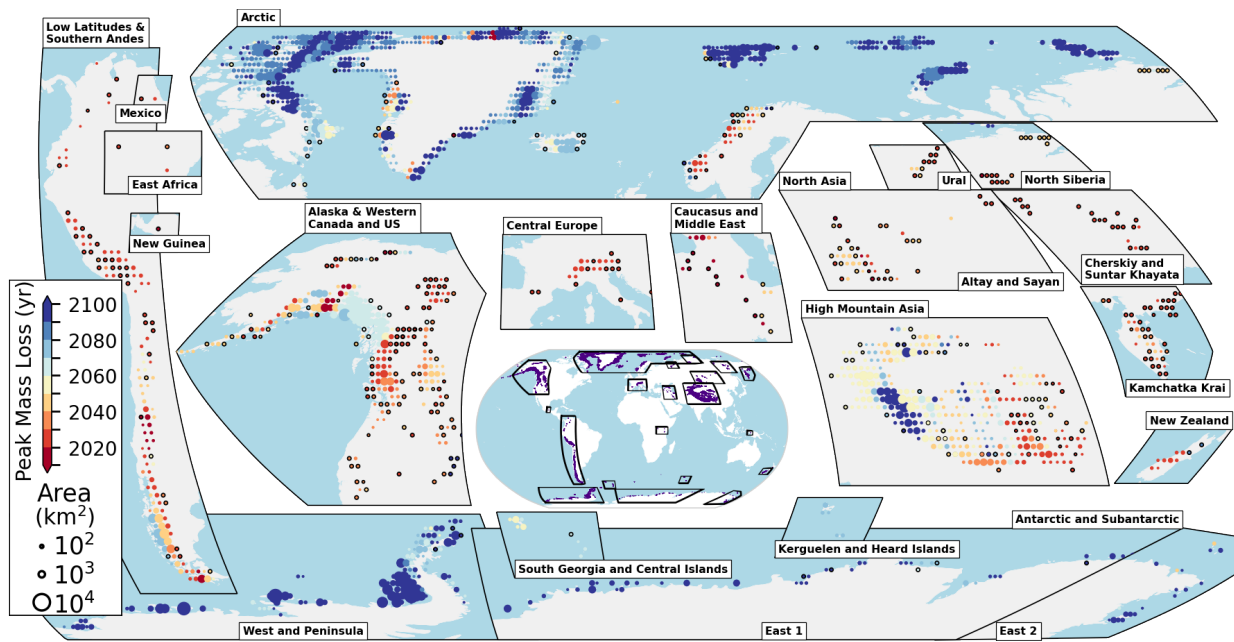


Fig. S7.

Spatial distribution of the year of maximum annual glacier mass loss (Gt) for +3°C. Tiles are aggregated by $1^\circ \times 1^\circ$ below 60° latitude, $2^\circ \times 1^\circ$ between 60° and 74° latitude and $2^\circ \times 2^\circ$ above 74° latitude to represent approximately 10,000 km 2 each. Circles are scaled based on glaciated area in 2015 and are colored by the year of maximum mass loss. Tiles that have experienced complete deglaciation by 2100 are marked by black circles. An 11-year running mean is used to reduce variability in individual years.

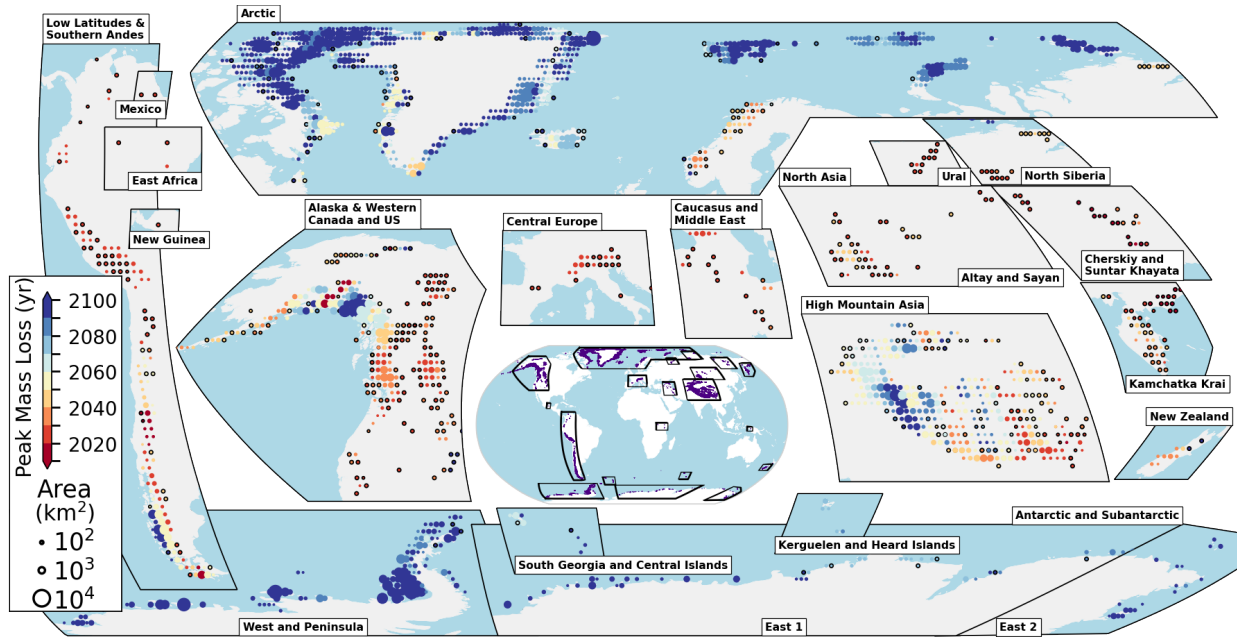


Fig. S8.

Spatial distribution of the year of maximum annual glacier mass loss (Gt) for +4°C. Tiles are aggregated by $1^\circ \times 1^\circ$ below 60° latitude, $2^\circ \times 1^\circ$ between 60° and 74° latitude and $2^\circ \times 2^\circ$ above 74° latitude to represent approximately 10,000 km^2 each. Circles are scaled based on glaciated area in 2015 and are colored by the year of maximum mass loss. Tiles that have experienced complete deglaciation by 2100 are marked by black circles. An 11-year running mean is used to reduce variability in individual years.

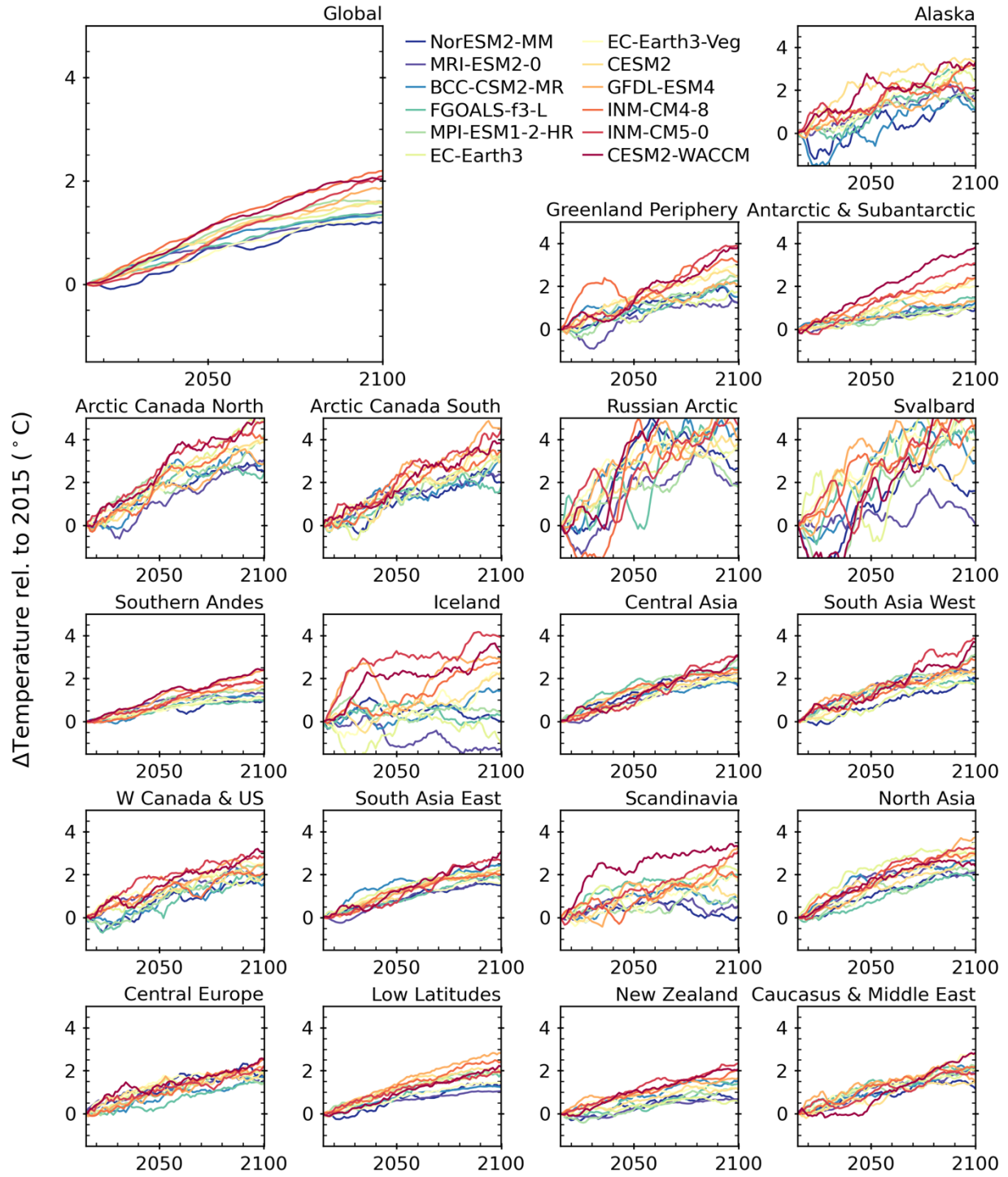


Fig. S9.

Global and regional projections of the annual temperature anomaly for glacierized regions from 2015 to 2100 for SSP2-4.5. Colors depict the GCMs. 11-year running mean used to reduce noise. Regions are ordered by their total mass loss.

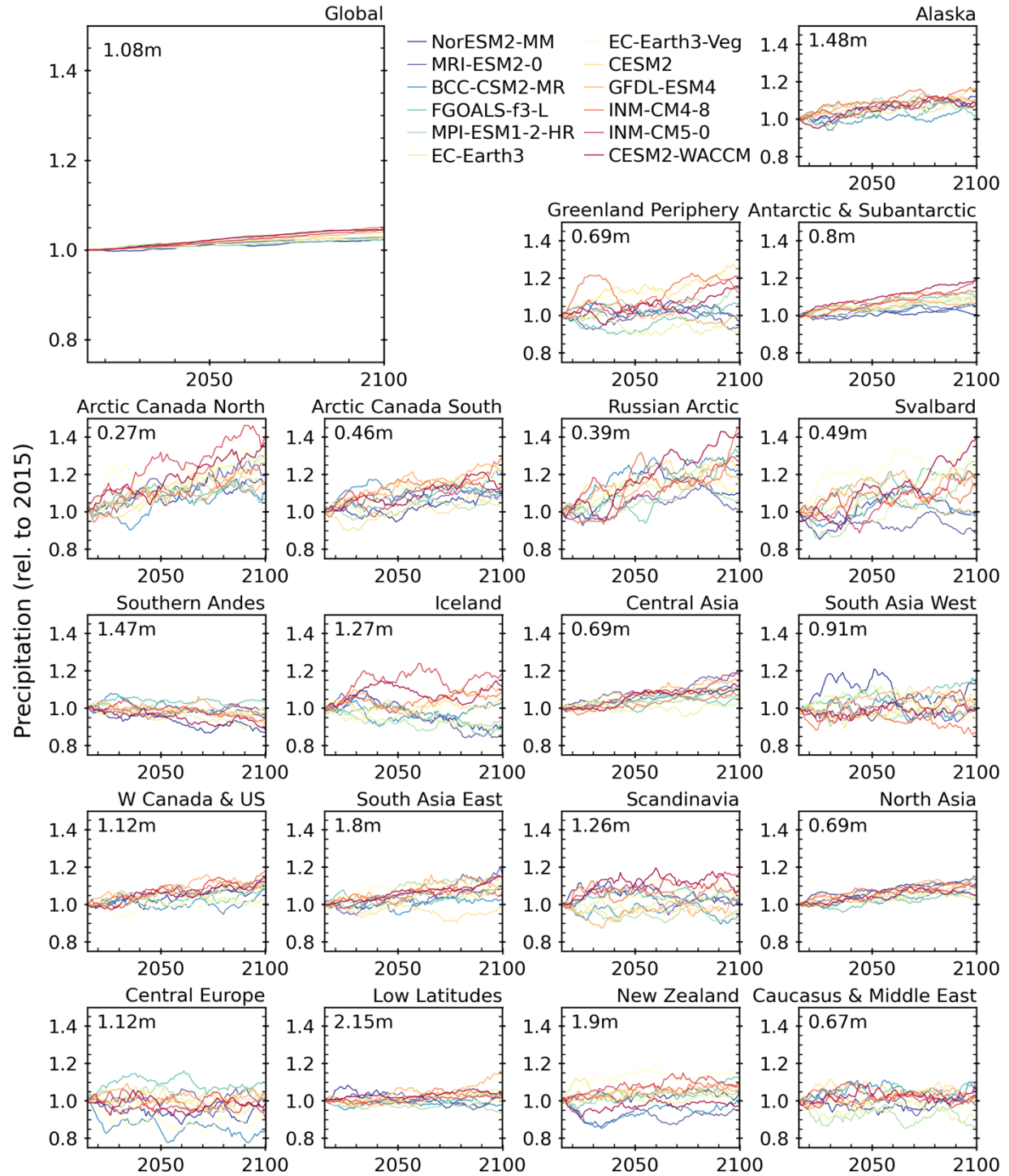


Fig. S10.

Global and regional projections of the annual precipitation anomaly for glacierized regions from 2015 to 2100 for SSP2-4.5. Colors depict the GCMs. 11-year running mean used to reduce noise. Text shows mean precipitation for each region of all GCMs in 2015. Regions are ordered by their total mass loss.

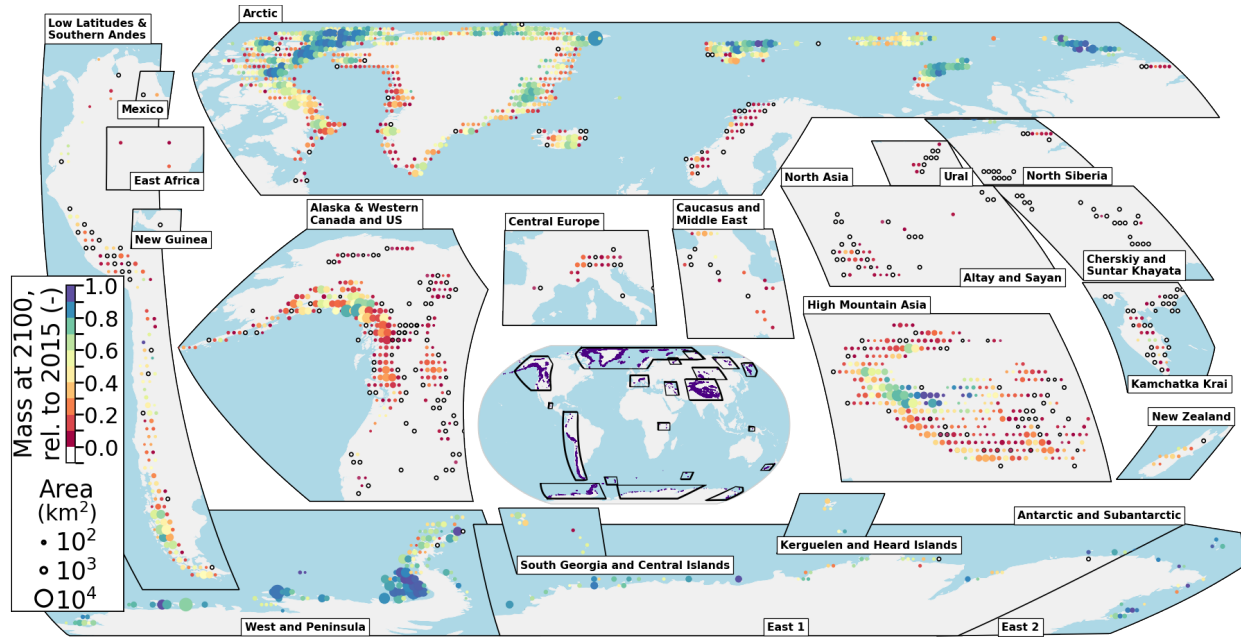


Fig. S11.

Spatial distribution of the ensemble median glacier mass remaining by 2100, relative to 2015, for the $+1.5^{\circ}\text{C}$ scenario. Tiles are aggregated by $1^{\circ} \times 1^{\circ}$ below 60° latitude, $2^{\circ} \times 1^{\circ}$ between 60° and 74° latitude and $2^{\circ} \times 2^{\circ}$ above 74° latitude to represent approximately $10,000 \text{ km}^2$ each. Circles are scaled based on simulated glaciated area in 2015 and are colored by normalized mass remaining. Tiles that have experienced complete deglaciation by 2100 are shown in white and outlined by a black circle.

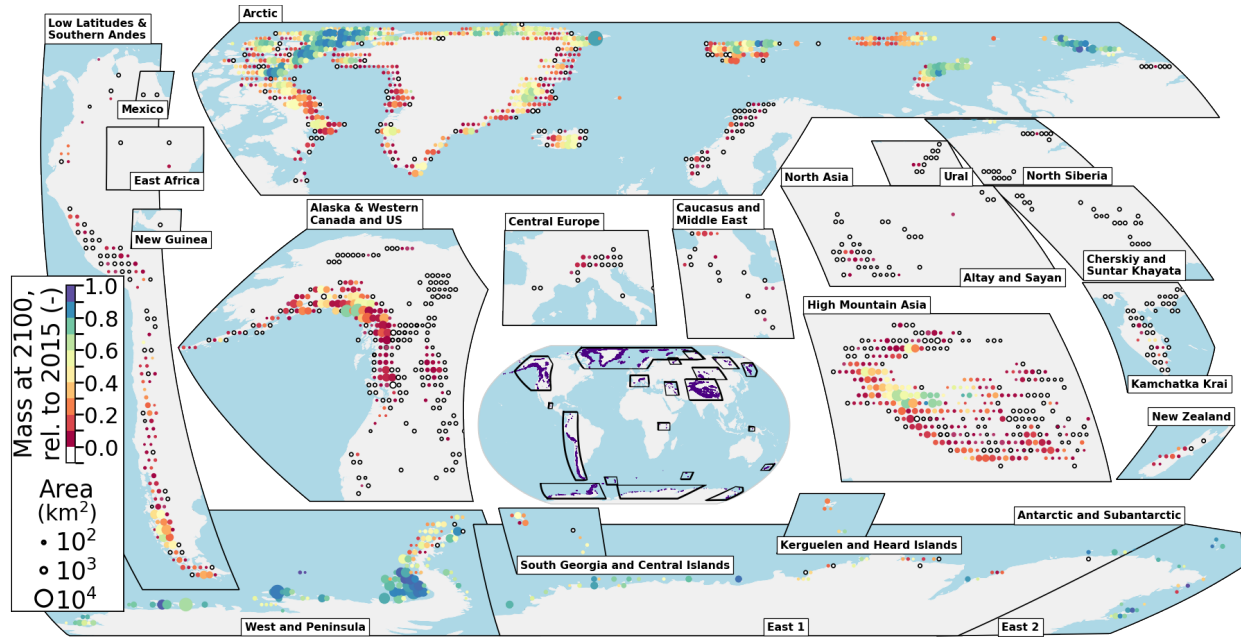


Fig. S12.

Spatial distribution of the ensemble median glacier mass remaining by 2100, relative to 2015, for the +3°C scenario. Tiles are aggregated by 1°x1° below 60° latitude, 2°x1° between 60° and 74° latitude and 2°x2° above 74° latitude to represent approximately 10,000 km² each. Circles are scaled based on simulated glacierized area in 2015 and are colored by normalized mass remaining. Tiles that have experienced complete deglaciation by 2100 are shown in white and outlined by a black circle.

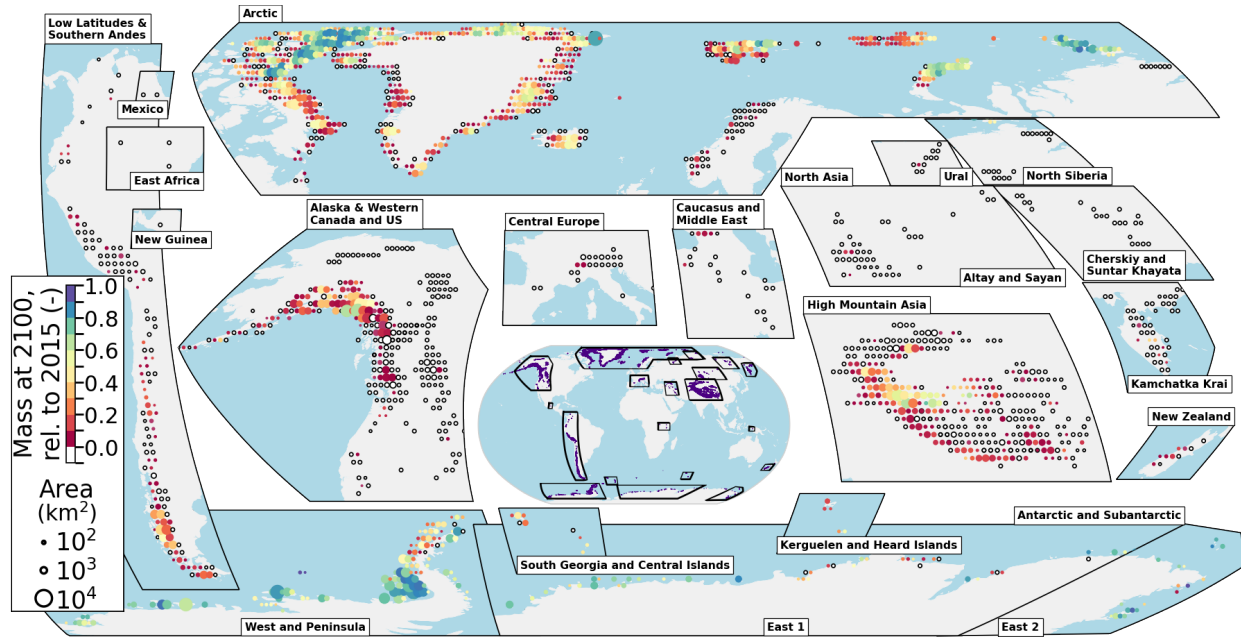


Fig. S13.

Spatial distribution of the ensemble median glacier mass remaining by 2100, relative to 2015, for the +4°C scenario. Tiles are aggregated by 1°x1° below 60° latitude, 2°x1° between 60° and 74° latitude and 2°x2° above 74° latitude to represent approximately 10,000 km² each. Circles are scaled based on simulated glacierized area in 2015 and are colored by normalized mass remaining. Tiles that have experienced complete deglaciation by 2100 are shown in white and outlined by a black circle.

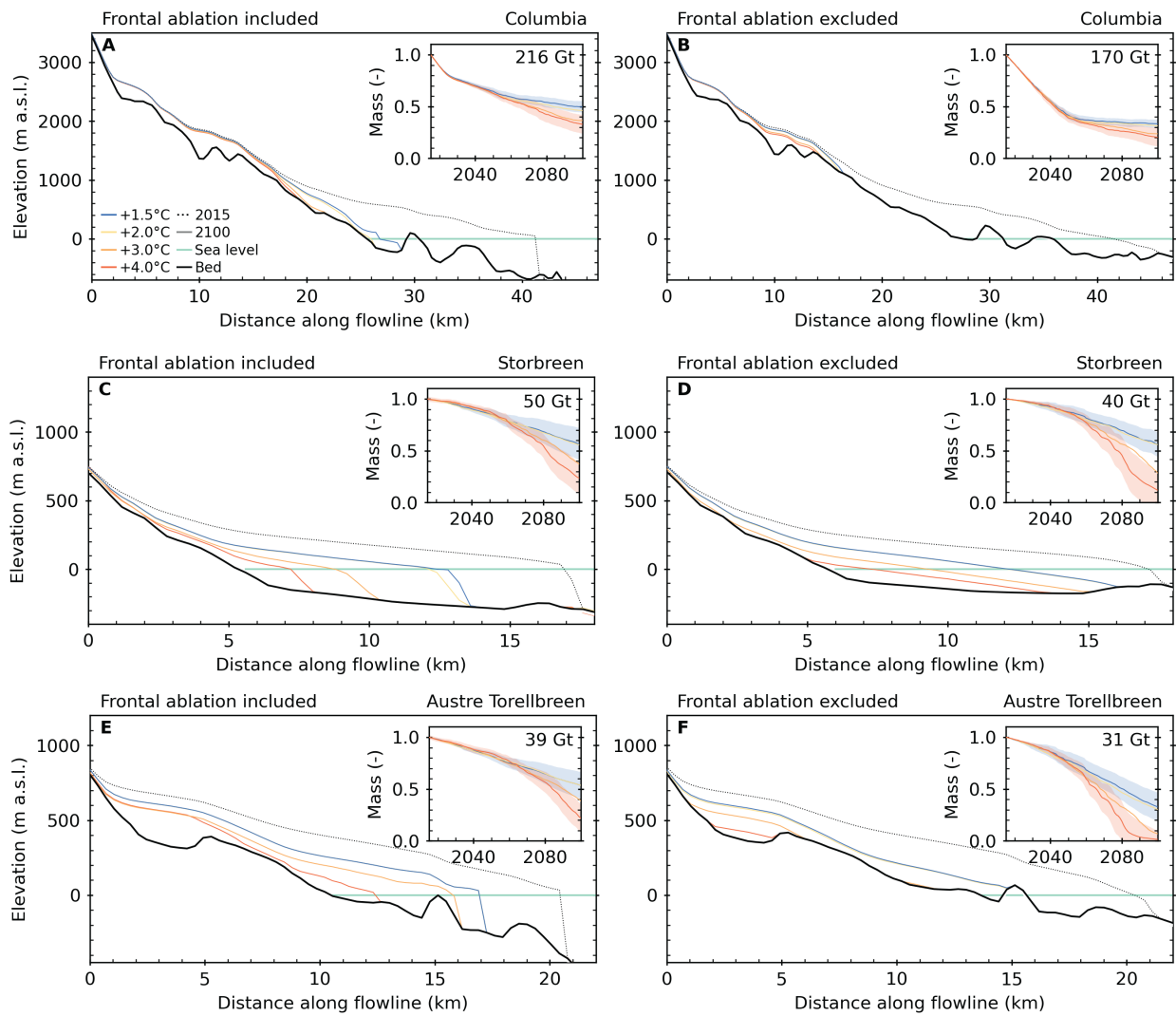


Fig. S14.

Impact of frontal ablation on projected mass change for Columbia Glacier, Alaska; Storbreen, Svalbard; and Austre Torellbreen, Svalbard. Surface elevation along the glacier flowline at 2100 for ensembles of temperature change scenarios (colored lines) with frontal ablation (A, C, E) included and (B, D, F) excluded in the simulations. Insets show mass change relative to 2015. Text shows the mass in Gt in 2015. The bed topography is internally derived for each model run so the ice thickness is consistent with the mass-balance gradient, and therefore differs between the two cases.

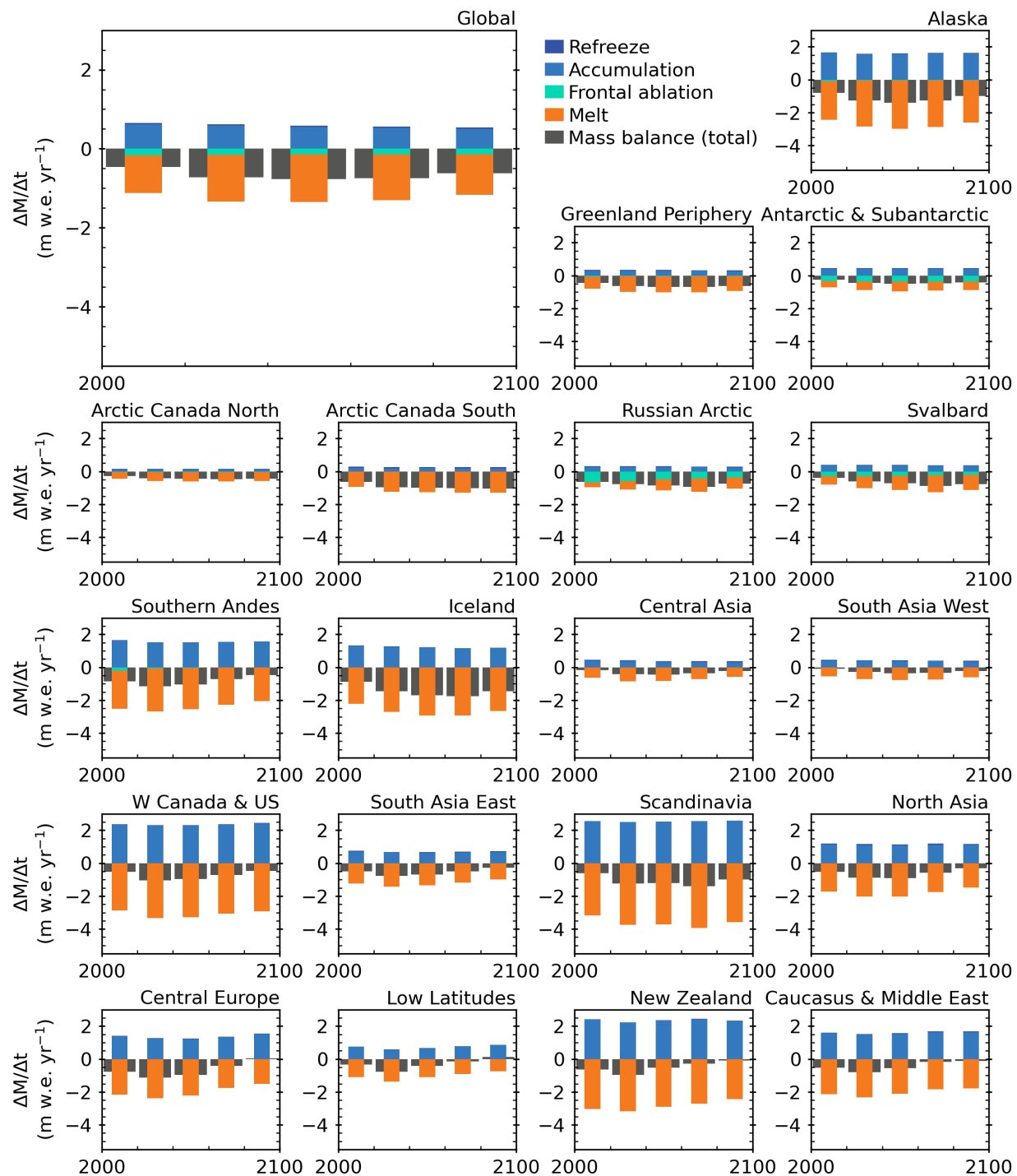


Fig. S15.

Global and regional mass balance components from 2000 to 2100 for the $+1.5^{\circ}\text{C}$ global mean temperature scenario by 2100 relative to pre-industrial levels. Components are averaged over 20-year periods. Regions are ordered by their total mass loss.

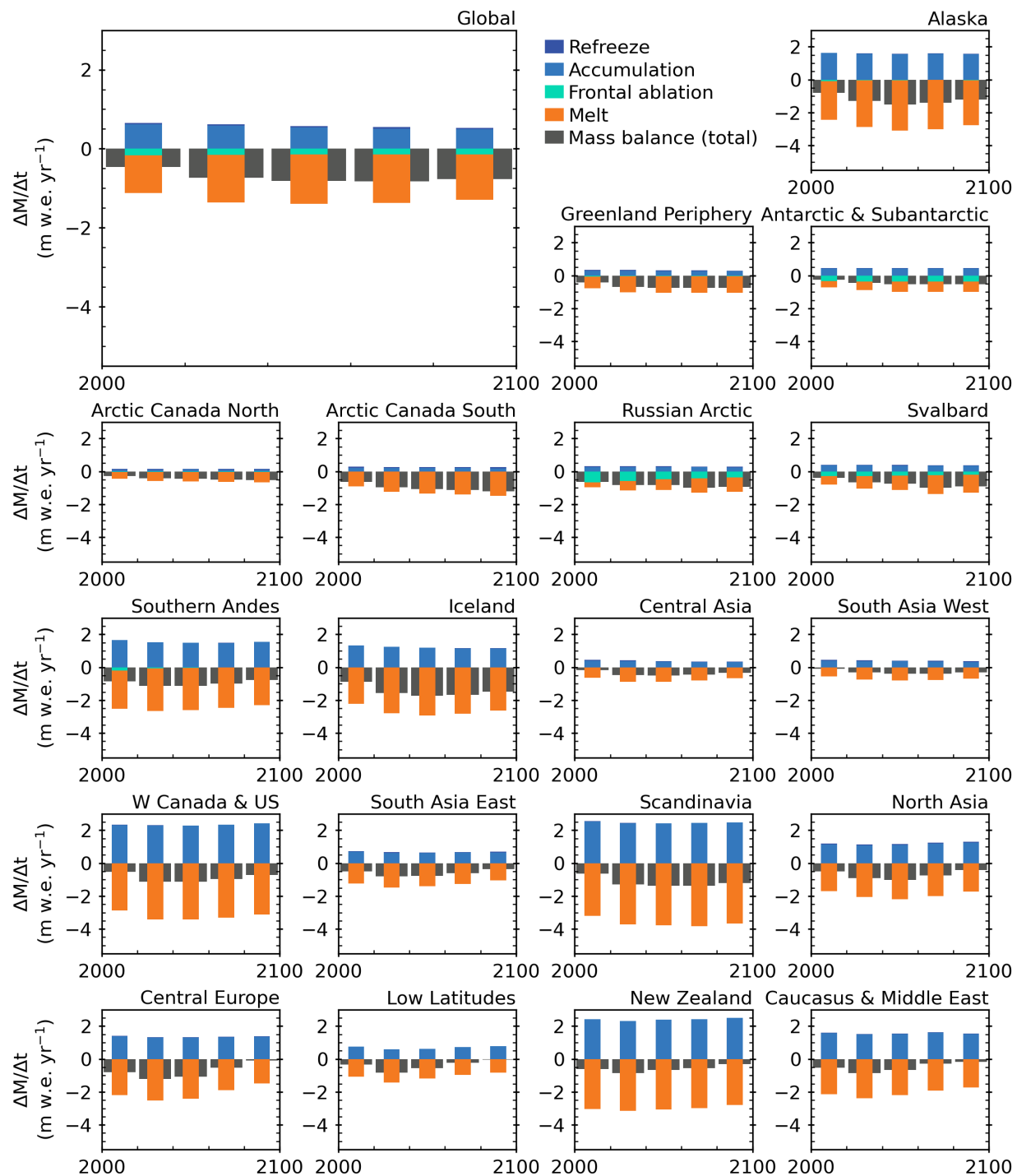


Fig. S16.

Global and regional mass balance components from 2000 to 2100 for the +2°C global mean temperature scenario by 2100 relative to pre-industrial levels. Components are averaged over 20-year periods. Regions are ordered by their total mass loss.

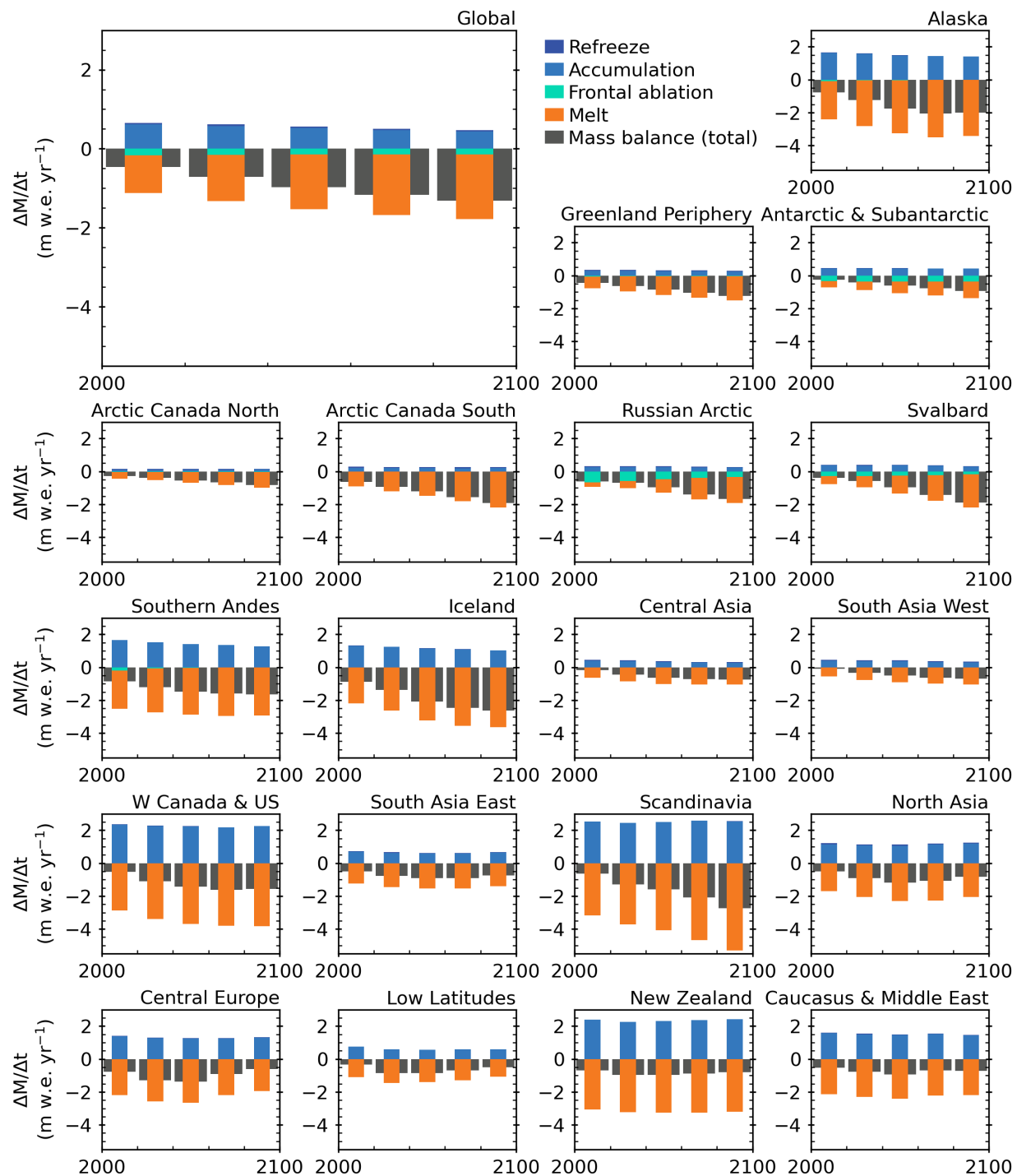


Fig. S17.

Global and regional mass balance components from 2000 to 2100 for the +3°C global mean temperature scenario by 2100 relative to pre-industrial levels. Components are averaged over 20-year periods. Regions are ordered by their total mass loss.

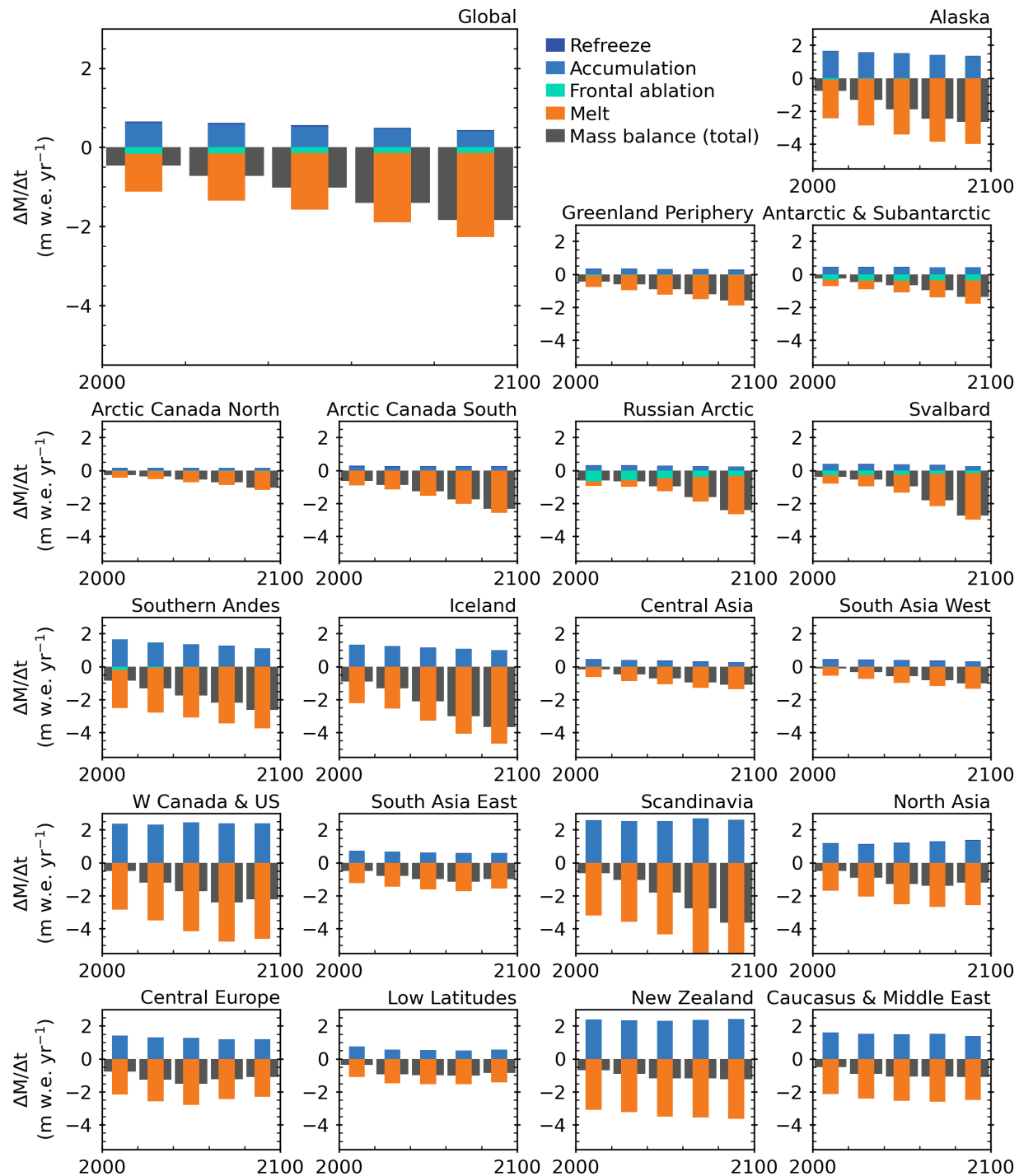


Fig. S18.

Global and regional mass balance components from 2000 to 2100 for the +4°C global mean temperature scenario by 2100 relative to pre-industrial levels. Components are averaged over 20-year periods. Regions are ordered by their total mass loss.

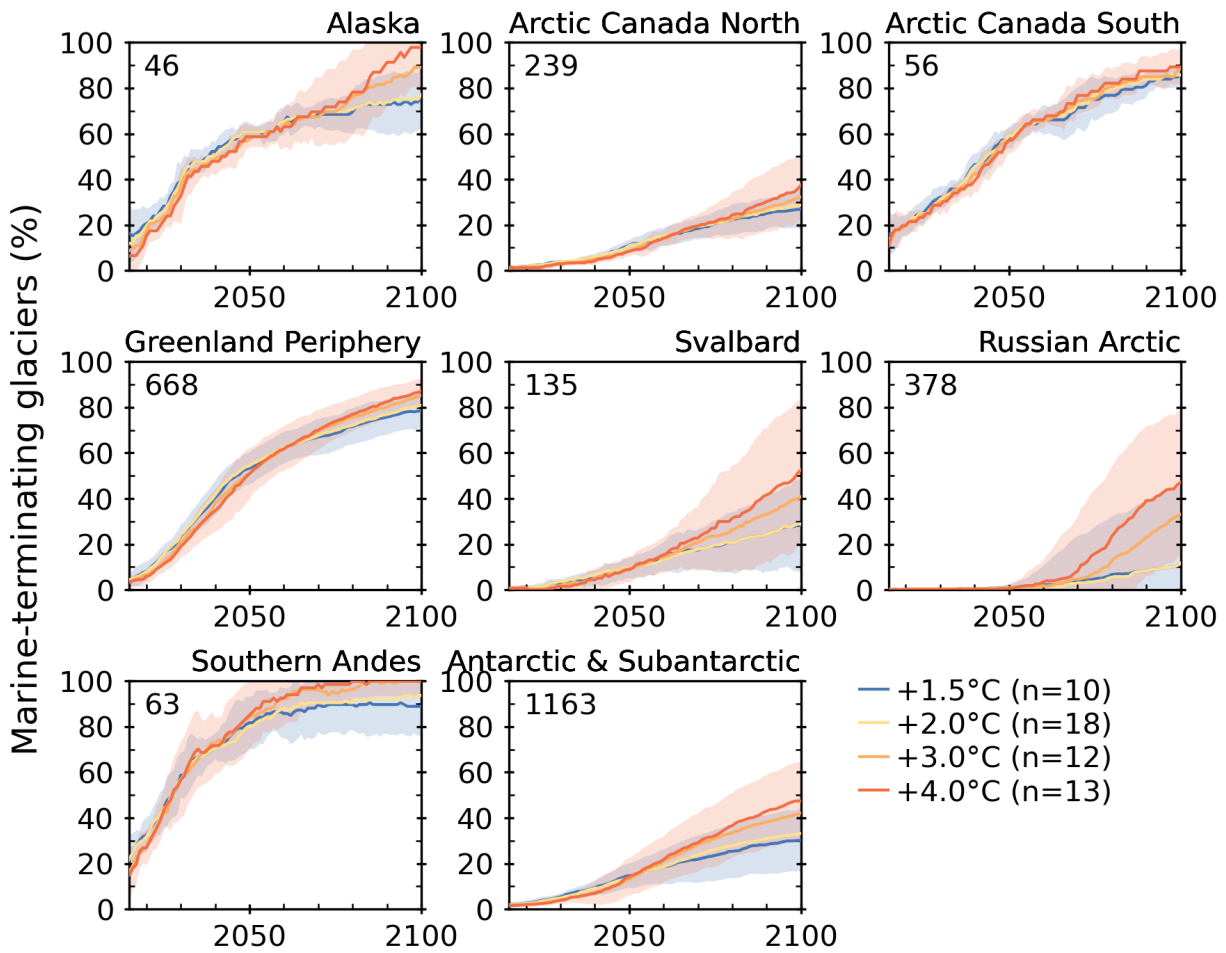


Fig. S19.

Regional percentage of marine-terminating glaciers that retreat to land from 2015 to 2100 for various temperature change scenarios. Four global mean temperature change scenarios are based on 2100 relative to pre-industrial levels. Text denotes the number of marine-terminating glaciers simulated in each region.

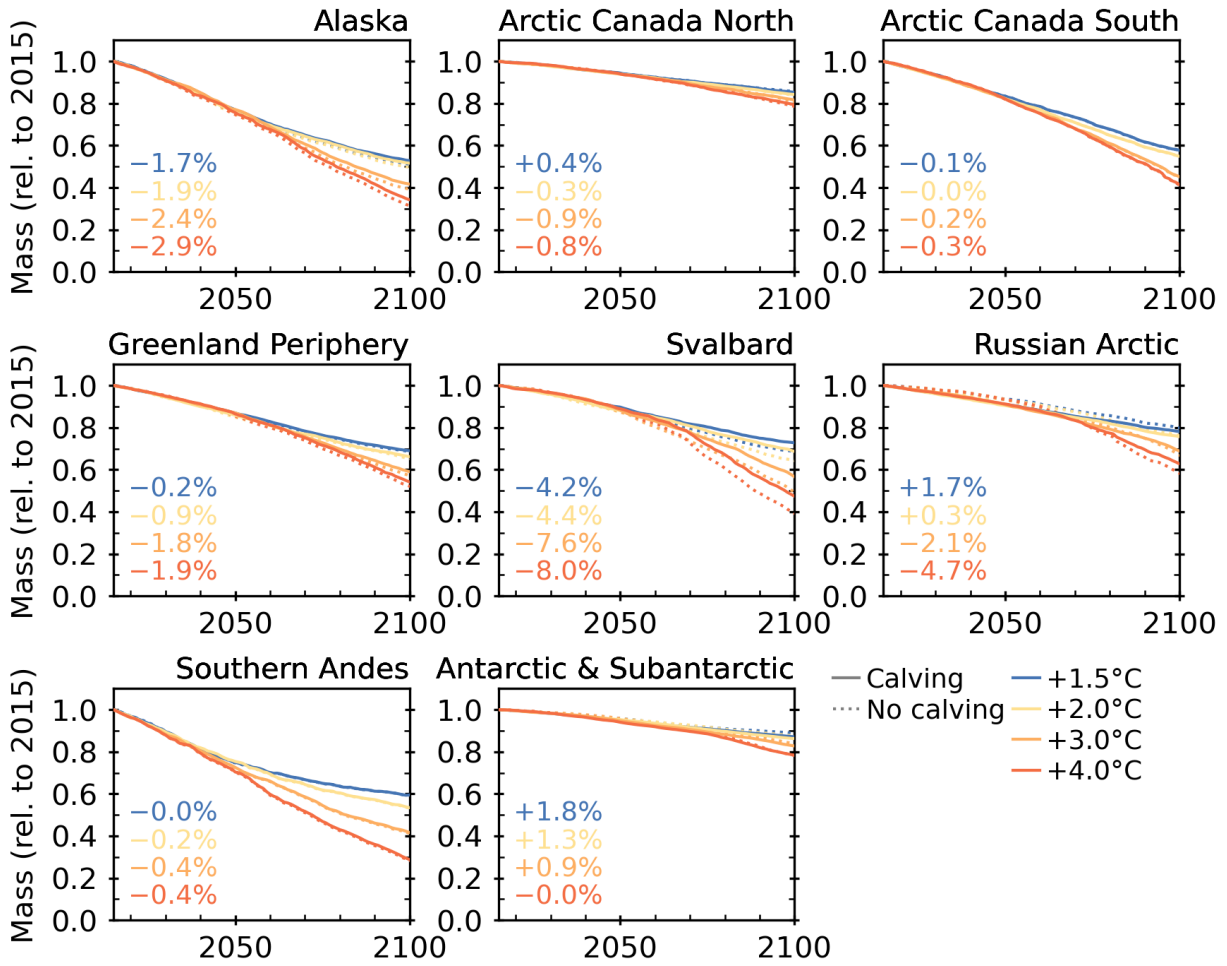


Fig. S20.

Impact of frontal ablation on projected mass change. Regional glacier mass evolution, relative to 2015, for four global mean temperature change scenarios by 2100 relative to pre-industrial levels (colors) accounting for frontal ablation (solid lines) and treating marine-terminating glaciers as land-terminating glaciers (dotted lines) for various regions with marine-terminating glaciers. Text shows the percent change of not accounting for frontal ablation compared to when it is included.

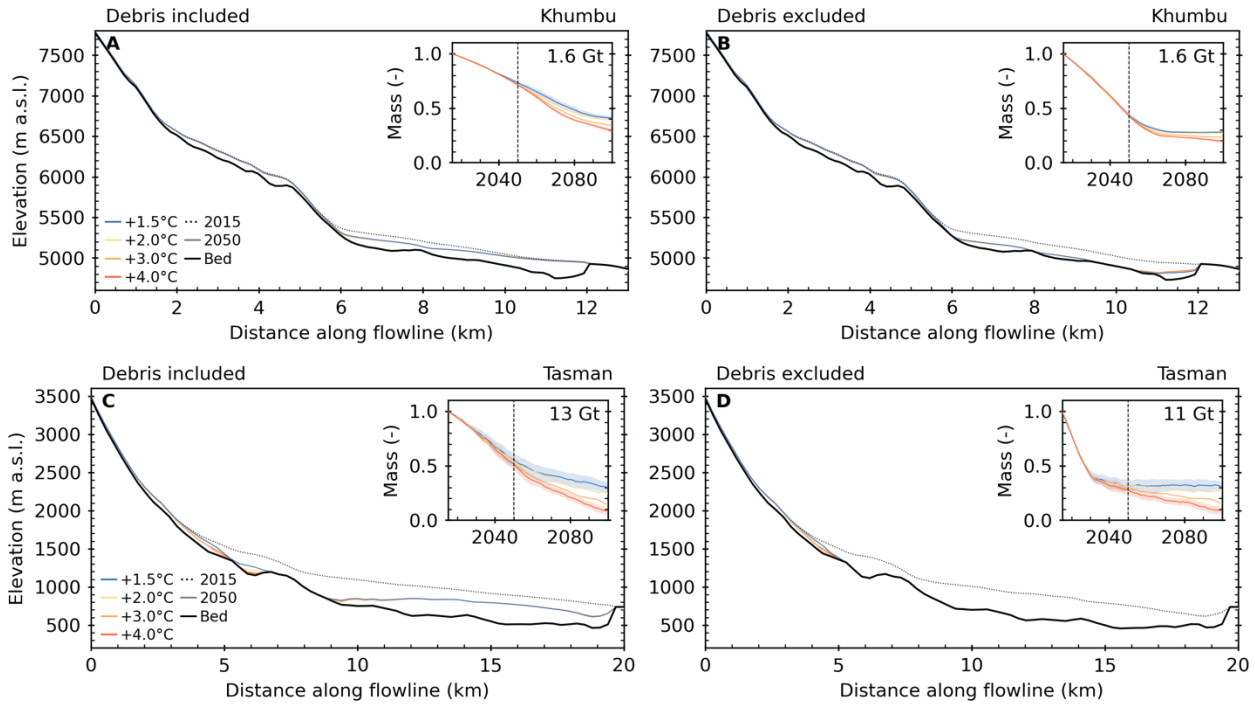


Fig. S21.

Impact of accounting for debris cover on projected mass change for Khumbu Glacier, Nepal and Tasman Glacier, New Zealand. Surface elevation along the glacier flowline at 2050 for ensembles of temperature change scenarios (colored lines) with debris (A, C) included and (B, D) excluded in the simulations. The cross sections are shown in 2050 to showcase the inverted mass balance gradient and separation of glacier tongues. Insets show mass change relative to 2015. Text shows the mass in Gt in 2015. The bed topography is internally derived for each model run so the ice thickness is consistent with the mass-balance gradient, and therefore the bed topography and initial mass differs between the two cases.

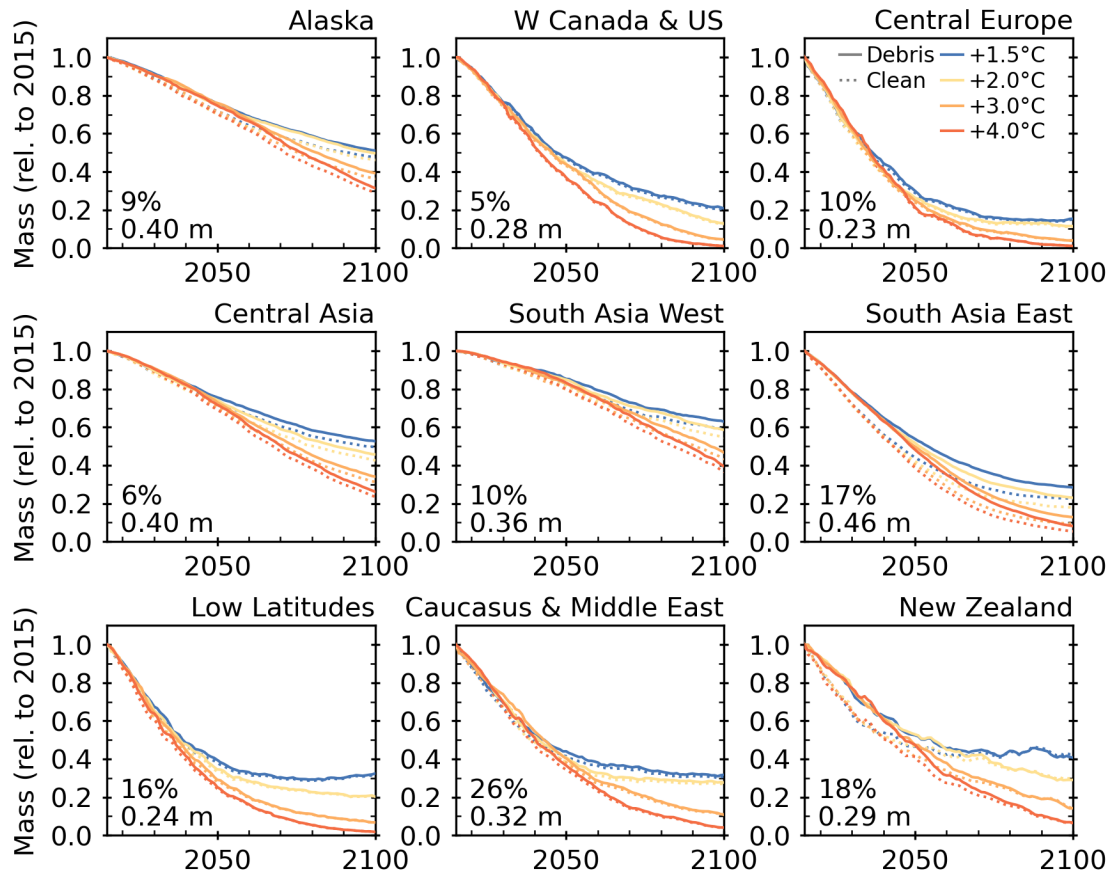


Fig. S22.

Impact of debris cover on projected mass change. Regional glacier mass evolution, relative to 2015, for four global mean temperature change scenarios by 2100 relative to pre-industrial levels accounting for debris compared to assuming clean ice in place of debris for various regions with significant debris-covered areas. Text shows the percent debris cover by area (24) and mean debris thickness (17).

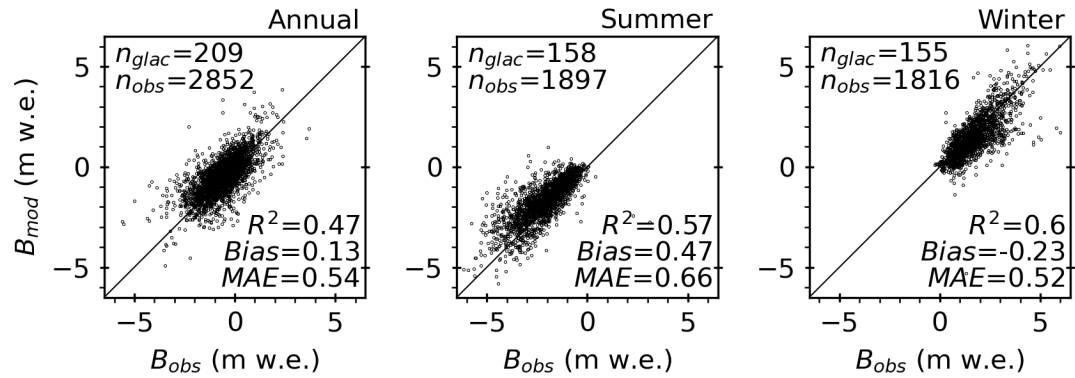


Fig. S23.

Validation of modeled glacier-wide mass balance (B_{mod}) compared to glaciological observations (B_{obs}) at annual and seasonal timescales (32). Validation for each region at annual and seasonal timescales are shown in Figs. S24-26. Bias and mean absolute error (MAE) shown in m w.e.

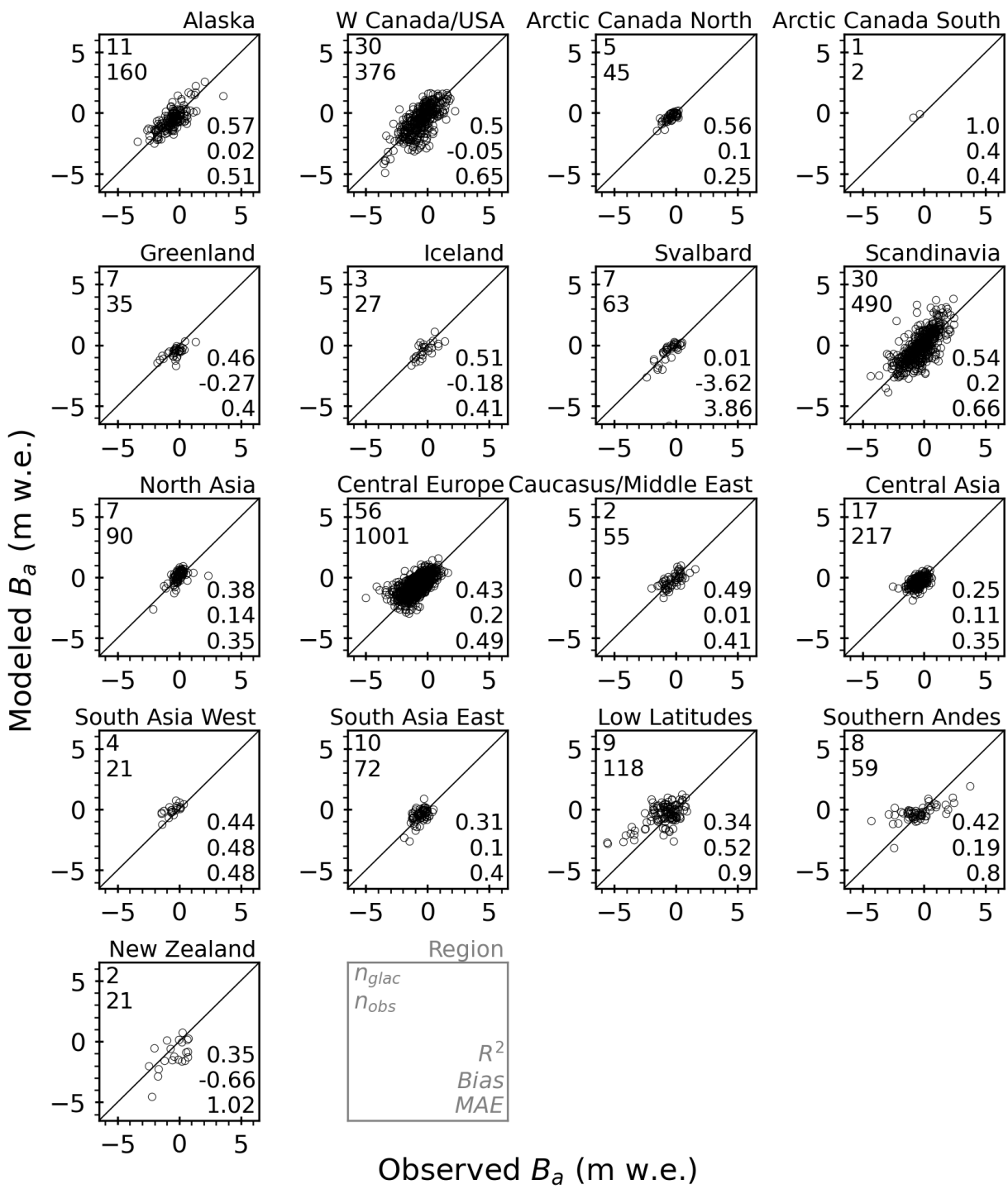


Fig. S24.

Validation of modeled annual glacier-wide mass balance (B_a) compared to glaciological observations for each region with data (32). The legend is in grey showing the number of glaciers (n_{glac}) and observations (n_{obs}) in upper left and correlation of determination (R^2), bias (m w.e. yr^{-1}), and mean absolute error (MAE; m w.e. yr^{-1}) in lower right.

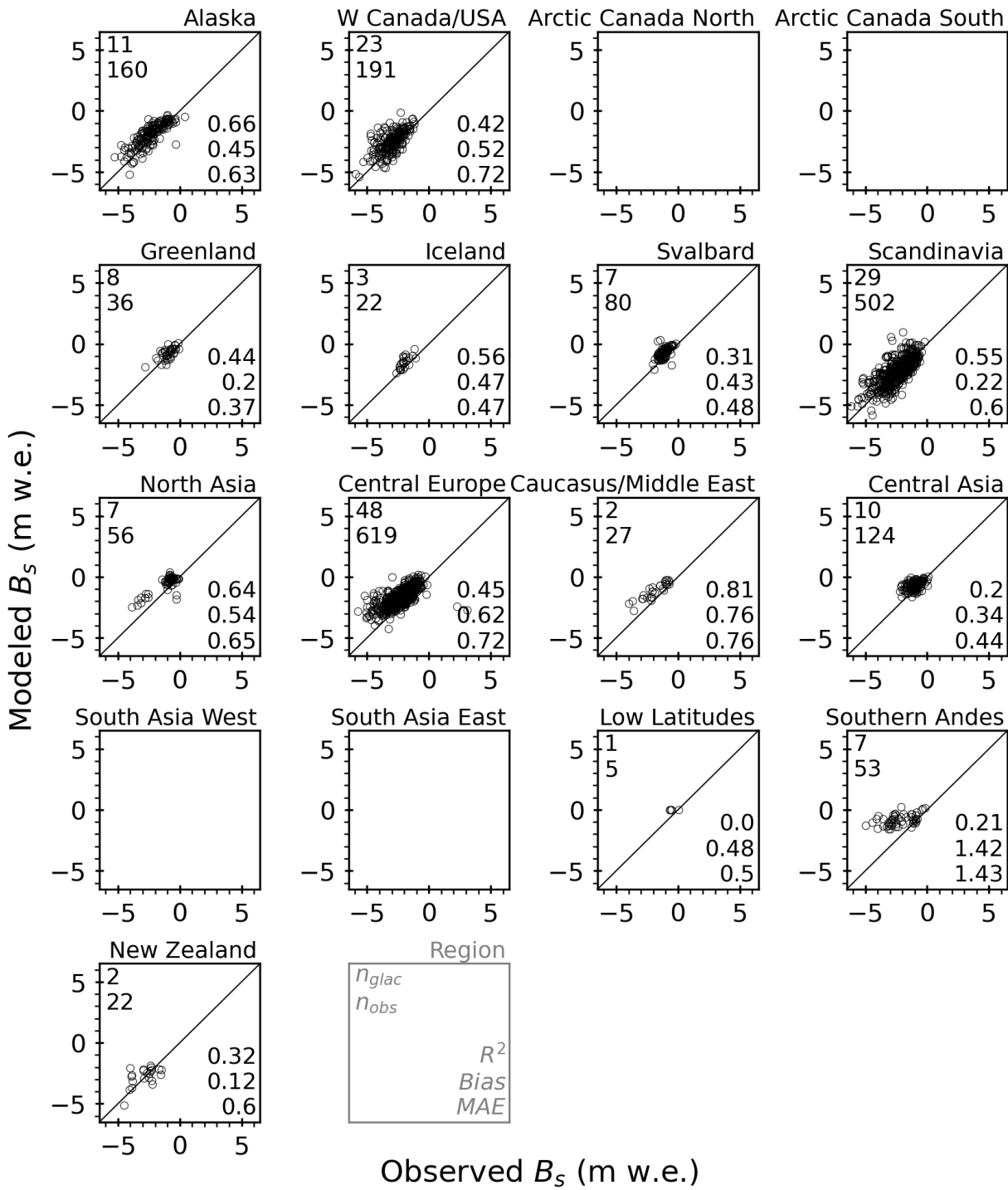


Fig. S25.

Validation of modeled summer glacier-wide mass balance (B_s) compared to glaciological observations for each region with data (32). Empty plots indicate regions with annual data, but no summer data. The legend is in grey showing the number of glaciers (n_{glac}) and observations (n_{obs}) in upper left and correlation of determination (R^2), bias (m w.e.), and mean absolute error (MAE; m w.e.) in lower right.

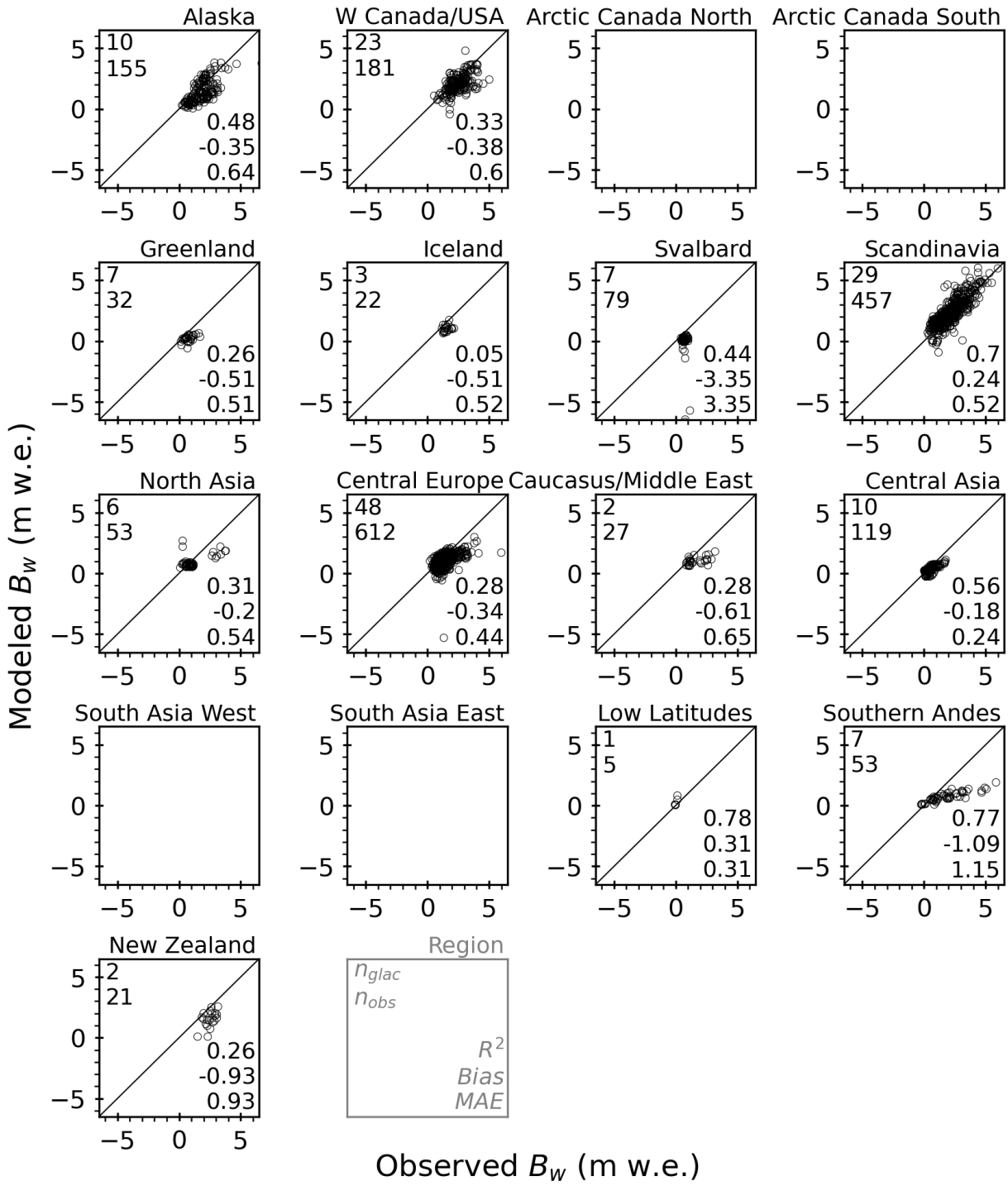


Fig. S26.

Validation of modeled winter glacier-wide mass balance (B_w) compared to glaciological observations for each region with data (32). Empty plots indicate regions with annual data, but no winter data. The legend is in grey showing the number of glaciers (n_{glac}) and observations (n_{obs}) in upper left and correlation of determination (R^2), bias (m w.e.), and mean absolute error (MAE; m w.e. yr^{-1}) in lower right.

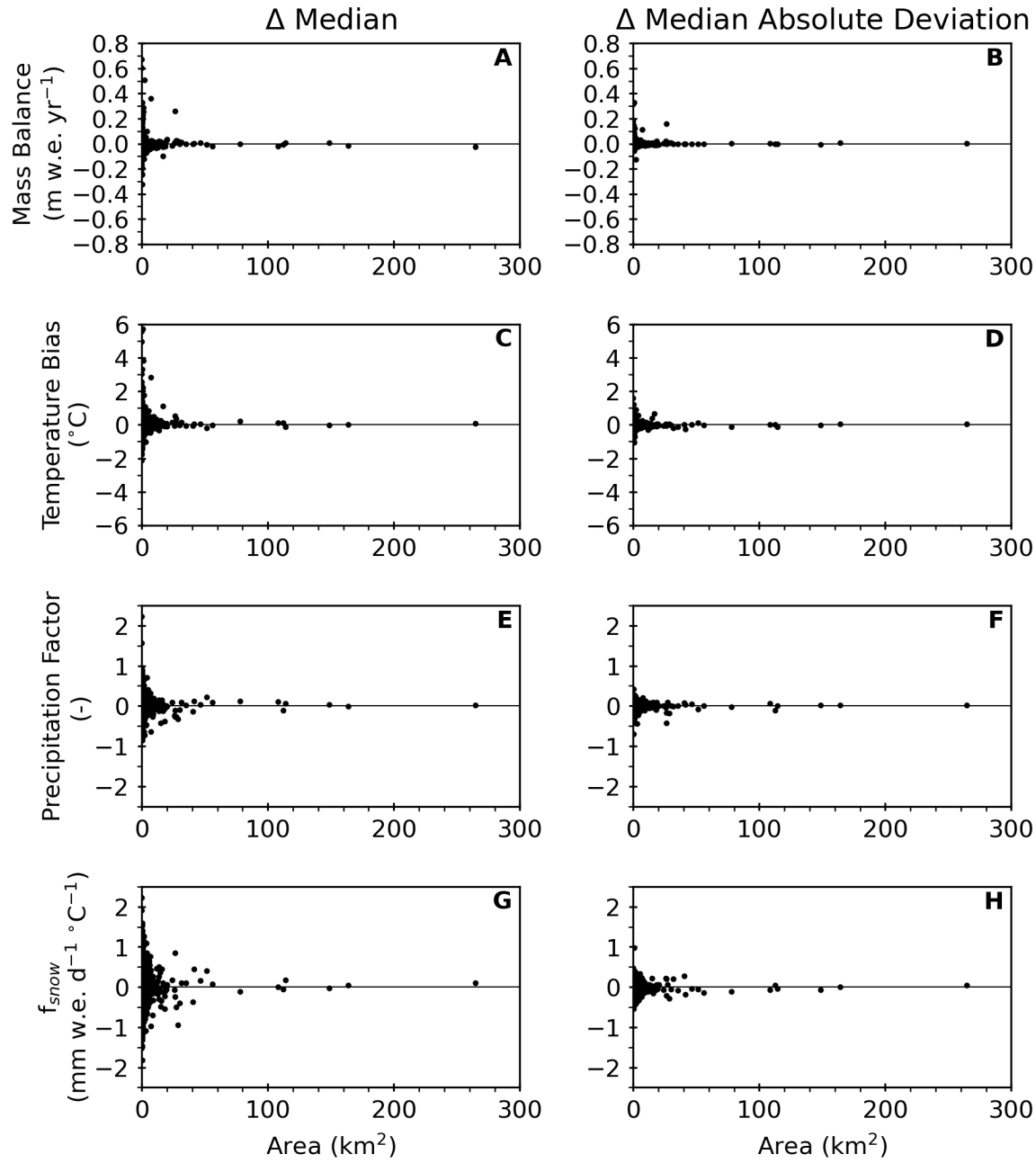


Fig. S27.

Comparison of posterior distributions as a function of glacier area when applying the Markov Monte Chain Methods using the emulator versus the full model. Differences in the median and median absolute deviation versus initial glacier area for the (A, B) posterior predictive distribution for the mass balance and marginal posterior distributions for the (C, D) temperature bias, (E, F) precipitation factor, and (G, H) degree-day factor of snow (f_{snow}) for 2500 randomly selected glaciers.

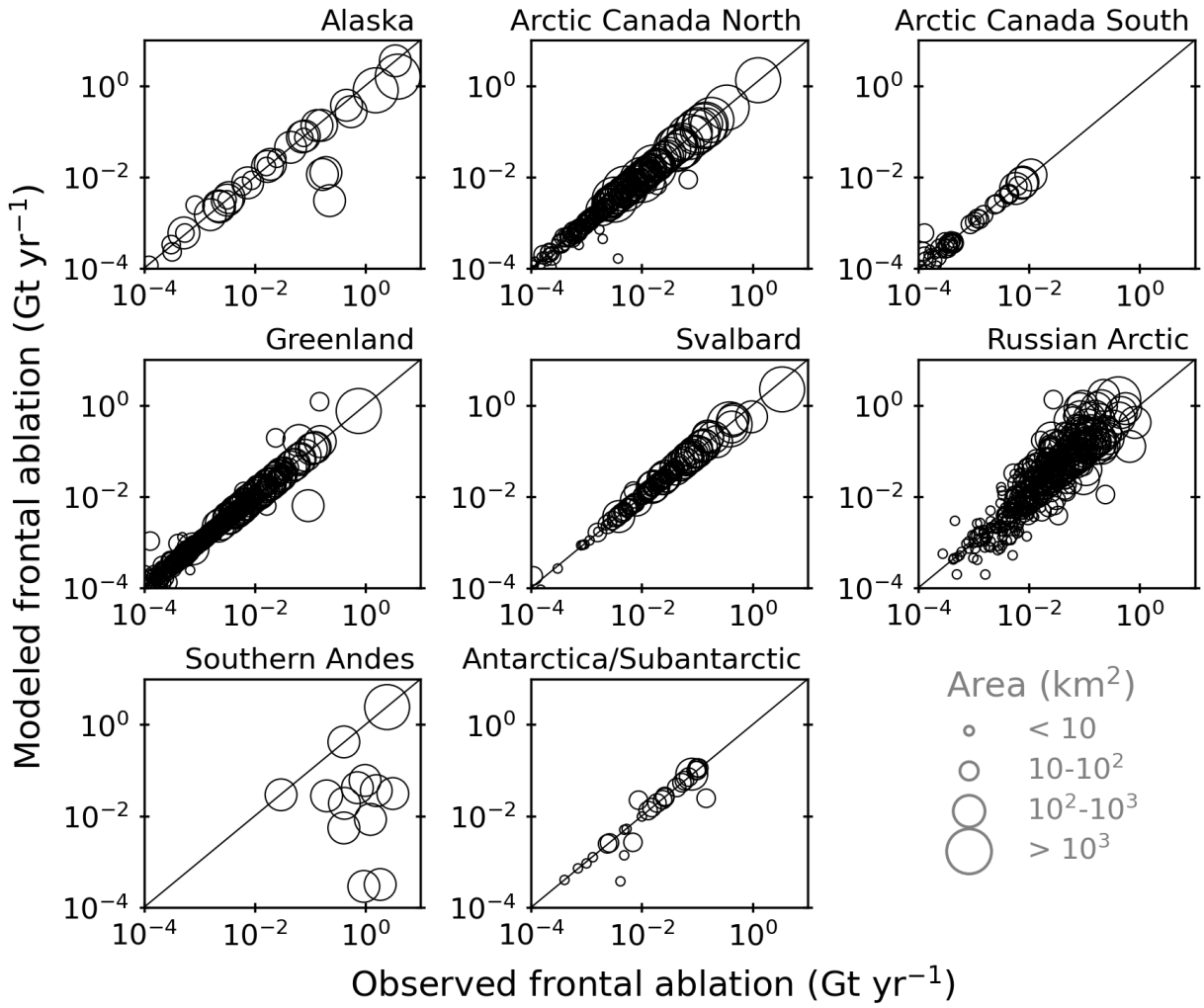


Fig. S28.

Comparison of modeled and observed frontal ablation rates of marine-terminating glaciers after calibration for each region with marine-terminating glaciers. Area refers to the area of each marine-terminating glacier.

Table S1.

Percentage of projected global and regional glacier mass loss by 2100, relative to 2015, for RCP scenarios from this study and a recent multi-model study (2). In 47 of the 57 regional cases, the regional relative mass losses (ensemble medians) are greater than the multi-model study (those greater than 15% are bolded). Note that uncertainty associated with Marzeion et al. (2) is expressed as 90% confidence interval based on up to 11 glacier models and 10 GCMs. This study reports ensemble median and 95% confidence interval. Projections for SSPs are shown in Table S5.

Region	RCP2.6		RCP4.5		RCP8.5	
	This study	Marzeion et al. (2)	This study	Marzeion et al. (2)	This study	Marzeion et al. (2)
Alaska	49±16	27±21	54±16	32±24	67±18	44±27
W Canada & US	76±21	64±30	94±19	78±29	99±6	90±23
Arctic Canada North	16±8	12±13	18±8	18±13	24±13	27±18
Arctic Canada South	41±26	23±27	46±26	33±30	63±24	48±32
Greenland Periphery	34±15	22±24	37±15	29±26	55±18	42±29
Iceland	38±27	30±35	50±34	40±47	62±37	55±45
Svalbard	27±12	35±34	39±29	50±36	57±33	66±36
Scandinavia	72±33	53±34	87±22	68±34	93±9	84±24
Russian Arctic	21±11	26±26	27±23	38±29	43±26	52±31
North Asia	77±22	62±41	87±10	79±38	95±5	90±30
Central Europe	78±14	68±31	93±9	83±22	99±3	95±13
Caucasus & Middle East	71±27	68±33	79±14	83±19	97±4	94±13
Central Asia	45±26	44±28	63±23	61±24	80±17	74±19
South Asia West	34±19	34±26	53±23	48±28	69±20	63±27
South Asia East	71±15	50±38	83±10	67±35	94±4	83±27
Low Latitudes	69±25	74±43	88±11	89±24	98±2	98±13
Southern Andes	38±15	23±27	49±17	30±27	68±20	46±26
New Zealand	53±25	44±45	74±18	58±33	93±9	79±27
Antarctic & Subantarctic	11±5	7±12	15±7	13±11	20±14	16±19
Global	26±8	18±13	31±10	27±15	43±13	36±20

Table S2.

Projected global and regional glacier contribution to sea-level rise (mm SLE) by 2100, relative to 2015, for RCP scenarios from this study and a recent multi-model study (2). Global excluding Greenland Periphery (G) and Antarctic and Subantarctic (A) are shown as well. ‘Uncorrected’ refers to the projections that assume mass losses below sea level contribute to sea-level rise, consistent with assumptions in the multi-model studies. Note that uncertainty associated with Marzeion et al. (2) is expressed as 90% confidence interval based on up to 11 glacier models and 10 GCMs. This study reports ensemble median and 95% confidence interval. Projections for SSPs are shown in Table S5.

Region	RCP2.6			RCP4.5			RCP8.5		
	This study	This study (uncorrected)	Marzeion et al. (2)	This study	This study (uncorrected)	Marzeion et al. (2)	This study	This study (uncorrected)	Marzeion et al. (2)
Alaska	22±8	22±8	14±11	24±8	25±8	19±13	31±9	31±9	25±15
W Canada & US	2±1	2±1	1±1	2±0	2±0	2±1	2±0	2±0	2±1
Arctic Canada North	11±6	12±7	10±10	12±6	13±6	16±15	17±10	19±11	24±20
Arctic Canada South	8±6	8±6	5±6	10±6	10±6	7±7	13±6	13±6	11±7
Greenland Periphery	12±6	13±6	9±10	13±6	14±6	12±11	21±7	22±8	18±11
Iceland	4±3	4±3	2±3	5±4	5±4	4±4	6±4	6±4	5±3
Svalbard	5±2	6±3	7±7	7±6	8±7	11±9	11±7	12±8	14±8
Scandinavia	0±0	0±0	0±0	1±0	1±0	0±0	1±0	1±0	0±0
Russian Arctic	5±4	9±5	10±8	8±9	12±11	14±11	14±10	19±13	20±12
North Asia	0±0	0±0	0±0	0±0	0±0	0±0	0±0	0±0	0±0
Central Europe	0±0	0±0	0±0	0±0	0±0	0±0	0±0	0±0	0±0
Caucasus & Middle East	0±0	0±0	0±0	0±0	0±0	0±0	0±0	0±0	0±0
Central Asia	4±2	4±2	4±3	5±2	5±2	6±3	7±2	7±2	6±4
South Asia West	2±1	2±1	3±2	4±2	4±2	4±2	5±2	5±2	5±3
South Asia East	1±0	1±0	1±1	2±0	2±0	2±1	2±0	2±0	2±1
Low Latitudes	0±0	0±0	0±0	0±0	0±0	0±0	0±0	0±0	0±0
Southern Andes	5±2	5±2	3±4	6±2	6±2	4±3	9±3	9±3	6±4
New Zealand	0±0	0±0	0±0	0±0	0±0	0±0	0±0	0±0	0±0
Antarctic & Subantarctic	6±5	15±7	9±15	10±7	20±10	16±13	15±14	27±21	20±24
Global (excl. A & G)	70±30	77±31	61±41	89±37	95±40	91±53	124±41	133±46	121±64
Global	90±36	106±37	79±56	114±44	132±47	119±66	163±53	187±61	159±86

Table S3.

Ensemble of GCMs, RCPs, and SSPs used to force the glacier evolution model from 2000-2100. In total, 82 climate projections were used.

Scenario	Number of GCMs	GCMs
SSP1-1.9	4	EC-Earth3, EC-Earth3-Veg, GFDL-ESM4, MRI-ESM2-0
SSP1-2.6		
SSP2-4.5	12	BCC-CSM2-MR, CESM2, CESM2-WACCM, EC-Earth3, EC-Earth3-Veg, FGOALS-f3-L, GFDL-ESM4, INM-CM4-8,
SSP3-7.0		INM-CM5-0, MPI-ESM1-2-HR, MRI-ESM2-0, NorESM2-MM
SSP5-8.5		
RCP2.6		CanESM2, CCSM4, CNRM-CM5, CSIRO-Mk3-6-0, GFDL-CM3,
RCP4.5	10	GFDL-ESM2M, GISS-E2-R, IPSL-CM5A-LR, MPI-ESM-LR,
RCP8.5		NorESM1-M

Table S4.

Global and regional ice volume in 2015 reporting ensemble median and 95% confidence interval.

Region	+1.5°C	+2°C	+3°C	+4°C
Alaska	18.45±0.45	18.62±0.50	18.75±0.28	18.92±0.39
W Canada & US	0.95±0.05	0.96±0.07	0.97±0.04	0.97±0.05
Arctic Canada North	29.15±1.09	29.40±1.33	29.89±1.66	30.39±1.54
Arctic Canada South	8.42±0.20	8.47±0.15	8.53±0.17	8.57±0.17
Greenland Periphery	15.42±0.37	15.55±0.43	15.76±0.44	15.90±0.33
Iceland	3.88±0.11	3.87±0.14	3.94±0.17	3.98±0.16
Svalbard	8.36±0.35	8.41±0.29	8.61±0.32	8.81±0.39
Scandinavia	0.28±0.01	0.28±0.01	0.28±0.01	0.28±0.01
Russian Arctic	17.58±0.57	17.72±0.50	17.91±0.55	18.17±0.55
North Asia	0.11±0.00	0.11±0.01	0.12±0.00	0.12±0.00
Central Europe	0.11±0.01	0.11±0.01	0.11±0.01	0.11±0.01
Caucasus & Middle East	0.05±0.00	0.05±0.00	0.05±0.00	0.05±0.00
Central Asia	3.20±0.06	3.25±0.09	3.32±0.06	3.39±0.05
South Asia West	2.76±0.05	2.79±0.09	2.86±0.08	2.92±0.07
South Asia East	0.77±0.01	0.78±0.02	0.79±0.02	0.80±0.01
Low Latitudes	0.09±0.00	0.09±0.01	0.09±0.00	0.09±0.00
Southern Andes	5.06±0.09	5.09±0.11	5.18±0.10	5.22±0.12
New Zealand	0.06±0.00	0.06±0.01	0.06±0.01	0.07±0.01
Antarctic & Subantarctic	54.10±1.39	54.36±1.49	55.50±1.78	56.59±1.79
Global	168.87±2.91	170.35±3.66	172.93±4.01	175.15±3.93

Table S5.

Percentage of projected global and regional glacier mass loss by 2100, relative to 2015, and glacier contribution to sea-level rise (mm SLE) from 2015 to 2100 for SSP scenarios. Global excluding Greenland Periphery (G) and Antarctic and Subantarctic (A) are shown as well. The reported values are the ensemble median and 95% confidence interval.

Region	Mass loss, relative to 2015 (%)				Sea level rise contribution, 2015-2100 (mm SLE)			
	SSP1-2.6	SSP2-4.5	SSP3-7.0	SSP5-8.5	SSP1-2.6	SSP2-4.5	SSP3-7.0	SSP5-8.5
Alaska	51±17	58±20	66±20	73±24	23±8	27±10	31±10	34±12
W Canada & US	87±13	95±8	99±5	99±3	2±0	2±0	2±0	2±0
Arctic Canada North	15±11	18±15	21±21	24±30	10±9	12±12	15±17	17±23
Arctic Canada South	45±15	53±17	60±21	66±27	9±3	11±4	13±5	14±6
Greenland Periphery	33±14	39±16	45±22	50±27	12±6	14±7	17±9	19±11
Iceland	39±23	48±26	55±26	62±27	4±2	5±3	5±3	6±3
Svalbard	29±22	37±28	49±31	64±29	5±4	7±6	9±7	12±6
Scandinavia	75±19	88±17	94±9	96±7	1±0	1±0	1±0	1±0
Russian Arctic	23±14	27±20	36±24	43±26	6±5	8±8	11±9	14±10
North Asia	81±10	89±6	93±5	95±4	0±0	0±0	0±0	0±0
Central Europe	86±8	95±4	99±2	100±1	0±0	0±0	0±0	0±0
Caucasus & Middle East	71±9	87±6	95±3	98±2	0±0	0±0	0±0	0±0
Central Asia	50±10	62±7	72±7	81±9	4±1	5±1	6±1	7±1
South Asia West	41±16	49±16	58±17	68±19	3±1	3±1	4±1	5±2
South Asia East	77±12	86±8	92±5	94±5	1±0	2±0	2±0	2±0
Low Latitudes	76±18	91±9	97±4	99±3	0±0	0±0	0±0	0±0
Southern Andes	49±19	57±19	68±21	74±22	6±3	7±3	9±3	9±3
New Zealand	64±21	80±13	93±8	95±7	0±0	0±0	0±0	0±0
Antarctic & Subantarctic	14±6	16±8	22±10	26±15	9±7	11±8	17±10	21±14
Global	28±9	32±12	39±15	44±20	98±38	116±51	147±64	166±83

References and Notes

1. R. Hugonnet, R. McNabb, E. Berthier, B. Menounos, C. Nuth, L. Girod, D. Farinotti, M. Huss, I. Dussaillant, F. Brun, A. Kääb, Accelerated global glacier mass loss in the early twenty-first century. *Nature* **592**, 726–731 (2021). [doi:10.1038/s41586-021-03436-z](https://doi.org/10.1038/s41586-021-03436-z) Medline
2. B. Marzeion, R. Hock, B. Anderson, A. Bliss, N. Champollion, K. Fujita, M. Huss, W. W. Immerzeel, P. Kraaijenbrink, J. H. Malles, F. Maussion, V. Radić, D. Rounce, A. Sakai, S. Shannon, R. van de Wal, H. Zekollari, Partitioning the Uncertainty of Ensemble Projections of Global Glacier Mass Change. *Earth's Futur.* **8**, (2020). [doi:10.1029/2019EF001470](https://doi.org/10.1029/2019EF001470)
3. W. W. Immerzeel, A. F. Lutz, M. Andrade, A. Bahl, H. Biemans, T. Bolch, S. Hyde, S. Brumby, B. J. Davies, A. C. Elmore, A. Emmer, M. Feng, A. Fernández, U. Haritashya, J. S. Kargel, M. Koppes, P. D. A. Kraaijenbrink, A. V. Kulkarni, P. A. Mayewski, S. Nepal, P. Pacheco, T. H. Painter, F. Pellicciotti, H. Rajaram, S. Rupper, A. Sinisalo, A. B. Shrestha, D. Vivioli, Y. Wada, C. Xiao, T. Yao, J. E. M. Baillie, Importance and vulnerability of the world's water towers. *Nature* **577**, 364–369 (2020). [doi:10.1038/s41586-019-1822-y](https://doi.org/10.1038/s41586-019-1822-y) Medline
4. M. Huss, R. Hock, Global-scale hydrological response to future glacier mass loss. *Nat. Clim. Chang.* **8**, 135–140 (2018). [doi:10.1038/s41558-017-0049-x](https://doi.org/10.1038/s41558-017-0049-x)
5. S. Harrison, J. S. Kargel, C. Huggel, J. Reynolds, D. H. Shugar, R. A. Betts, A. Emmer, N. Glasser, U. K. Haritashya, J. Klimeš, L. Reinhardt, Y. Schaub, A. Wiltshire, D. Regmi, V. Vilímek, Climate change and the global pattern of moraine-dammed glacial lake outburst floods. *Cryosphere* **12**, 1195–1209 (2018). [doi:10.5194/tc-12-1195-2018](https://doi.org/10.5194/tc-12-1195-2018)
6. T. L. Edwards, S. Nowicki, B. Marzeion, R. Hock, H. Goelzer, H. Seroussi, N. C. Jourdain, D. A. Slater, F. E. Turner, C. J. Smith, C. M. McKenna, E. Simon, A. Abe-Ouchi, J. M. Gregory, E. Larour, W. H. Lipscomb, A. J. Payne, A. Shepherd, C. Agosta, P. Alexander, T. Albrecht, B. Anderson, X. Asay-Davis, A. Aschwanden, A. Barthel, A. Bliss, R. Calov, C. Chambers, N. Champollion, Y. Choi, R. Cullather, J. Cuzzone, C. Dumas, D. Felikson, X. Fettweis, K. Fujita, B. K. Galton-Fenzi, R. Gladstone, N. R. Golledge, R. Greve, T. Hattermann, M. J. Hoffman, A. Humbert, M. Huss, P. Huybrechts, W. Immerzeel, T. Kleiner, P. Kraaijenbrink, S. Le Clec'h, V. Lee, G. R. Leguy, C. M. Little, D. P. Lowry, J.-H. Malles, D. F. Martin, F. Maussion, M. Morlighem, J. F. O'Neill, I. Nias, F. Pattyn, T. Pelle, S. F. Price, A. Quiquet, V. Radić, R. Reese, D. R. Rounce, M. Rückamp, A. Sakai, C. Shafer, N.-J. Schlegel, S. Shannon, R. S. Smith, F. Straneo, S. Sun, L. Tarasov, L. D. Trusel, J. Van Breedam, R. van de Wal, M. van den Broeke, R. Winkelmann, H. Zekollari, C. Zhao, T. Zhang, T. Zwinger, Projected land ice contributions to twenty-first-century sea level rise. *Nature* **593**, 74–82 (2021). [doi:10.1038/s41586-021-03302-y](https://doi.org/10.1038/s41586-021-03302-y) Medline
7. F. Maussion, A. Butenko, N. Champollion, M. Dusch, J. Eis, K. Fourteau, P. Gregor, A. H. Jarosch, J. Landmann, F. Oesterle, B. Recinos, T. Rothenpieler, A. Vlug, C. T. Wild, B. Marzeion, The Open Global Glacier Model (OGGM) v1.1. *Geosci. Model Dev.* **12**, 909–931 (2019). [doi:10.5194/gmd-12-909-2019](https://doi.org/10.5194/gmd-12-909-2019)
8. M. Huss, R. Hock, A new model for global glacier change and sea-level rise. *Front. Earth Sci.* **3**, (2015). [doi:10.3389/feart.2015.00054](https://doi.org/10.3389/feart.2015.00054)

9. R. Hock, A. Bliss, B. E. N. Marzeion, R. H. Giesen, Y. Hirabayashi, M. Huss, V. Radic, A. B. A. Slanger, GlacierMIP-A model intercomparison of global-scale glacier mass-balance models and projections. *J. Glaciol.* **65**, 453–467 (2019). [doi:10.1017/jog.2019.22](https://doi.org/10.1017/jog.2019.22)
10. B. Osmanoğlu, M. Braun, R. Hock, F. J. Navarro, Surface velocity and ice discharge of the ice cap on King George Island, Antarctica. *Ann. Glaciol.* **54**, 111–119 (2013). [doi:10.3189/2013AoG63A517](https://doi.org/10.3189/2013AoG63A517)
11. B. Osmanoglu, F. J. Navarro, R. Hock, M. Braun, M. I. Corcuera, Surface velocity and mass balance of Livingston Island ice cap, Antarctica. *Cryosphere* **8**, 1807–1823 (2014). [doi:10.5194/tc-8-1807-2014](https://doi.org/10.5194/tc-8-1807-2014)
12. M. Minowa, M. Schaefer, S. Sugiyama, D. Sakakibara, P. Skvarca, Frontal ablation and mass loss of the Patagonian icefields. *Earth Planet. Sci. Lett.* **561**, 116811 (2021). [doi:10.1016/j.epsl.2021.116811](https://doi.org/10.1016/j.epsl.2021.116811)
13. W. Kochtitzky, L. Copland, W. Van Wychen, R. Hugonnet, R. Hock, J. A. Dowdeswell, T. Benham, T. Strozzi, A. Glazovsky, I. Lavrentiev, D. R. Rounce, R. Millan, A. Cook, A. Dalton, H. Jiskoot, J. Cooley, J. Jania, F. Navarro, The unquantified mass loss of Northern Hemisphere marine-terminating glaciers from 2000-2020. *Nat. Commun.* **13**, 5835 (2022). [doi:10.1038/s41467-022-33231-x](https://doi.org/10.1038/s41467-022-33231-x) [Medline](#)
14. D. R. Rounce, T. Khurana, M. B. Short, R. Hock, D. E. Shean, D. J. Brinkerhoff, Quantifying parameter uncertainty in a large-scale glacier evolution model using Bayesian inference: Application to High Mountain Asia. *J. Glaciol.* **66**, 175–187 (2020). [doi:10.1017/jog.2019.91](https://doi.org/10.1017/jog.2019.91)
15. D. R. Rounce, R. Hock, D. E. Shean, Glacier Mass Change in High Mountain Asia Through 2100 Using the Open-Source Python Glacier Evolution Model (PyGEM). *Front. Earth Sci.* **7**, 331 (2020). [doi:10.3389/feart.2019.00331](https://doi.org/10.3389/feart.2019.00331)
16. K. Hutter, The Effect of Longitudinal Strain on the Shear Stress of an Ice Sheet: In Defence of Using Stretched Coordinates. *J. Glaciol.* **27**, 39–56 (1981). [doi:10.1017/S0022143000011217](https://doi.org/10.1017/S0022143000011217)
17. D. R. Rounce, R. Hock, R. W. McNabb, R. Millan, C. Sommer, M. H. Braun, P. Malz, F. Maussion, J. Mouginot, T. C. Seehaus, D. E. Shean, Distributed Global Debris Thickness Estimates Reveal Debris Significantly Impacts Glacier Mass Balance. *Geophys. Res. Lett.* **48**, GL091311 (2021). [doi:10.1029/2020GL091311](https://doi.org/10.1029/2020GL091311) [Medline](#)
18. D. Farinotti, M. Huss, J. J. Fürst, J. Landmann, H. Machguth, F. Maussion, A. Pandit, A consensus estimate for the ice thickness distribution of all glaciers on Earth. *Nat. Geosci.* **12**, 168–173 (2019). [doi:10.1038/s41561-019-0300-3](https://doi.org/10.1038/s41561-019-0300-3)
19. R. Hock, G. Rasul, C. Adler, B. Cáceres, S. Gruber, Y. Hirabayashi, M. Jackson, A. Kääb, S. Kang, S. Kutuzov, A. Milner, U. Molau, S. Morin, B. Orlove, H. Steltzer, “High Mountain Areas” in *IPCC Special Report on the Ocean and Cryosphere in a Changing Climate*, H.-O. Pörtner, D. C. Roberts, V. Masson-Delmotte, P. Zhai, M. Tignor, E. Poloczanska, K. Mintenbeck, A. Alegría, M. Nicolai, A. Okem, J. Petzold, B. Rama, N. M. Weyer, Eds. (Cambridge University Press, 2019).
20. H. Zekollari, M. Huss, D. Farinotti, Modelling the future evolution of glaciers in the European Alps under the EURO-CORDEX RCM ensemble. *Cryosphere* **13**, 1125–1146 (2019). [doi:10.5194/tc-13-1125-2019](https://doi.org/10.5194/tc-13-1125-2019)

21. F. Pithan, T. Mauritsen, Arctic amplification dominated by temperature feedbacks in contemporary climate models. *Nat. Geosci.* **7**, 181–184 (2014). [doi:10.1038/ngeo2071](https://doi.org/10.1038/ngeo2071)
22. J. Bolibar, A. Rabatel, I. Gouttevin, H. Zekollari, C. Galiez, Nonlinear sensitivity of glacier mass balance to future climate change unveiled by deep learning. *Nat. Commun.* **13**, 409 (2022). [doi:10.1038/s41467-022-28033-0](https://doi.org/10.1038/s41467-022-28033-0) Medline
23. RGI Consortium, Randolph glacier inventory - A dataset of global glacier outlines, Version 6.0, GLIMS (2017); <https://doi.org/10.7265/4m1f-gd79>.
24. D. Scherler, H. Wulf, N. Gorelick, Global Assessment of Supraglacial Debris-Cover Extents. *Geophys. Res. Lett.* **45**, 11798–11805 (2018). [doi:10.1029/2018GL080158](https://doi.org/10.1029/2018GL080158)
25. S. Herreid, F. Pellicciotti, The state of rock debris covering Earth’s glaciers. *Nat. Geosci.* **13**, 621–627 (2020). [doi:10.1038/s41561-020-0615-0](https://doi.org/10.1038/s41561-020-0615-0)
26. G. Østrem, Ice melting under a thin layer of moraine, and the existence of ice cores in moraine ridges. *Geogr. Ann.* **41**, 228–230 (1959).
27. D. I. Benn, T. Bolch, K. Hands, J. Gulley, A. Luckman, L. I. Nicholson, D. Quincey, S. Thompson, R. Toumi, S. Wiseman, Response of debris-covered glaciers in the Mount Everest region to recent warming, and implications for outburst flood hazards. *Earth Sci. Rev.* **114**, 156–174 (2012). [doi:10.1016/j.earscirev.2012.03.008](https://doi.org/10.1016/j.earscirev.2012.03.008)
28. A.V. Rowan, D. L. Egholm, D. J. Quincey, B. Hubbard, O. King, E. S. Miles, K. E. Miles, J. Hornsey, The Role of Differential Ablation and Dynamic Detachment in Driving Accelerating Mass Loss From a Debris-Covered Himalayan Glacier. *J. Geophys. Res. Earth Surf.* **126**, (2021). [doi:10.1029/2020JF005761](https://doi.org/10.1029/2020JF005761)
29. K. B. Tokarska, M. B. Stolpe, S. Sippel, E. M. Fischer, C. J. Smith, F. Lehner, R. Knutti, Past warming trend constrains future warming in CMIP6 models *Sci. Adv.* **6**, aaz9549 (2020). [doi:10.1126/sciadv.aaz9549](https://doi.org/10.1126/sciadv.aaz9549).
30. K. Wyser, E. Kjellström, T. Koenigk, H. Martins, R. Döscher, Warmer climate projections in EC-Earth3-Veg: The role of changes in the greenhouse gas concentrations from CMIP5 to CMIP6. *Environ. Res. Lett.* **15**, 054020 (2020). [doi:10.1088/1748-9326/ab81c2](https://doi.org/10.1088/1748-9326/ab81c2)
31. UNEP, “Emissions Gap Report 2021” (UNEP, 2021); <https://www.unep.org/emissions-gap-report-2021>).
32. WGMS, Fluctuations of Glaciers Database (World Glacier Monitoring Service, 2021), https://www.gtn-g.ch/data_catalogue_fog/.
33. H. Hersbach, B. Bell, P. Berrisford, S. Hirahara, A. Horányi, J. Muñoz-Sabater, J. Nicolas, C. Peubey, R. Radu, D. Schepers, A. Simmons, C. Soci, S. Abdalla, X. Abellan, G. Balsamo, P. Bechtold, G. Biavati, J. Bidlot, M. Bonavita, G. de Chiara, P. Dahlgren, D. Dee, M. Diamantakis, R. Dragani, J. Flemming, R. Forbes, M. Fuentes, A. Geer, L. Haimberger, S. Healy, R. J. Hogan, E. Hólm, M. Janisková, S. Keeley, P. Laloyaux, P. Lopez, C. Lupu, G. Radnoti, P. de Rosnay, I. Rozum, F. Vamborg, S. Villaume, J. N. Thépaut, The ERA5 global reanalysis. *Q. J. R. Meteorol. Soc.* **146**, 1999–2049 (2020). [doi:10.1002/qj.3803](https://doi.org/10.1002/qj.3803)
34. P. A. Arias, N. Bellouin, E. Coppola, R. G. Jones, G. Krinner, J. Marotzke, V. Naik, M. D. Palmer, G.-K. Plattner, J. Rogelj, M. Rojas, J. Sillmann, T. Storelvmo, P. W. Thorne, B. Trewin, K. Achuta Rao, B. Adhikary, R. P. Allan, K. Armour, G. Bala, R. Barimalala, S.

Berger, J. G. Canadell, C. Cassou, A. Cherchi, W. Collins, W. D. Collins, S. L. Connors, S. Corti, F. Cruz, F. J. Dentener, C. Dereczynski, A. di Luca, A. Diongue Niang, F. J. Doblas-Reyes, A. Dosio, H. Douville, F. Engelbrecht, V. Eyring, E. Fischer, P. Forster, B. Fox-Kemper, J. S. Fuglestvedt, J. C. Fyfe, N. P. Gillet, L. Goldfarb, I. Gorodetskaya, J. M. Gutierrez, R. Hamdi, E. Hawkins, H. T. Heewitt, P. Hope, A. S. Islam, C. Jones, D. S. Kaufman, R. E. Kopp, Y. Kosaka, J. Kossin, S. Krakovska, J.-Y. Lee, J. Li, T. Mauritzen, T. K. Maycock, M. Meinshausen, S.-K. Min, P. M. S. Monteiro, T. Ngo-Duc, F. Otto, I. Pinto, A. Pirani, K. Raghavan, R. Ranasinghe, A. C. Ruane, L. Ruiz, J.-B. Sallée, B. H. Samset, S. Sathyendranath, S. I. Seneviratne, A. A. Sörensson, S. Szopa, I. Takayabu, A.-M. Trguier, B. van den Hurk, R. Vautard, K. von Schuckmann, S. Zaehle, X. Zhang, K. Zickfeld, “Technical Summary” in *Climate Change 2021: The Physical Science Basis. Contribution of Working Group 1 to the Sixth Assessment Report of the Intergovernmental Panel on Climate Change*, V. Masson-Delmotte, P. Zhai, A. Pirani, S. L. Connors, C. Péan, S. Berger, N. Caud, Y. Chen, L. Goldfarb, M. I. Gomis, M. Huang, K. Leitzell, E. Lonnoy, J. B. R. Matthews, T. K. Maycock, T. Waterfield, O. Yelekci, R. Yu, B. Zhou, Eds. (Cambridge Univ. Press, 2021).

35. J. Oerlemans, F. M. Nick, A minimal model of a tidewater glacier. *Ann. Glaciol.* **42**, 1–6 (2005). [doi:10.3189/172756405781813023](https://doi.org/10.3189/172756405781813023)
36. J. G. Cogley, R. Hock, L. A. Rasmussen, A. A. Arendt, A. Bauder, R. J. Braithwaite, P. Jansso, G. Kaser, M. Möller, L. Nicholson, M. Zemp, “Glossary of Glacier Mass Balance and Related Terms” (IHP-VII Technical Documents in Hydrology No. 86, IACS Contribution No. 2, 2011); https://wgms.ch/downloads/Cogley_et.al_2011.pdf
37. C. E. Rasmussen, C. K. I. Williams, *Gaussian Processes for Machine Learning* (MIT Press, 2006).
38. D. P. Kingma, J. Ba, Adam: A Method for Stochastic Optimization. [arXiv:0706.1234](https://arxiv.org/abs/0706.1234) [cs.LG] (2014).
39. R. J. Braithwaite, Temperature and precipitation climate at the equilibrium-line altitude of glaciers expressed by the degree-day factor for melting snow. *J. Glaciol.* **54**, 437–444 (2008). [doi:10.3189/002214308785836968](https://doi.org/10.3189/002214308785836968)
40. R. Millan, J. Mouginot, A. Rabatel, M. Morlighem, Ice velocity and thickness of the world’s glaciers. *Nat. Geosci.* **15**, 124–129 (2022). [doi:10.1038/s41561-021-00885-z](https://doi.org/10.1038/s41561-021-00885-z)
41. B. Recinos, F. Maussion, T. Rothenpieler, B. Marzeion, Impact of frontal ablation on the ice thickness estimation of marine-terminating glaciers in Alaska. *Cryosphere* **13**, 2657–2672 (2019). [doi:10.5194/tc-13-2657-2019](https://doi.org/10.5194/tc-13-2657-2019)